Veneers, rinds, and fracture fills: Relatively late alteration of sedimentary rocks at Meridiani Planum, Mars

Andrew H. Knoll,[1] Brad L. Jolliff,[2] William H. Farrand,[3] James F. Bell III,[4] Benton C. Clark,[5] Ralf Gellert,[6,7] M. P. Golombek,[8] John P. Grotzinger,[9] Kenneth E. Herkenhoff,[10] Jeffrey R. Johnson,[10] Scott M. McLennan,[11] Richard Morris,[12] Steven W. Squyres,[4] Robert Sullivan,[4] Nicholas J. Tosca,[11,13] Albert Yen,[8] and Zoe Learner[4]

Received 1 June 2007; revised 7 September 2007; accepted 10 January 2008; published 8 May 2008.

[1] Veneers and thicker rinds that coat outcrop surfaces and partially cemented fracture fills formed perpendicular to bedding document relatively late stage alteration of ancient sedimentary rocks at Meridiani Planum, Mars. The chemistry of submillimeter thick, buff-colored veneers reflects multiple processes at work since the establishment of the current plains surface. Veneer composition is dominated by the mixing of silicate-rich dust and sulfate-rich outcrop surface, but it has also been influenced by mineral precipitation, including NaCl, and possibly by limited physical or chemical weathering of sulfate minerals. Competing processes of chemical alteration (perhaps mediated by thin films of water or water vapor beneath blanketing soils) and sandblasting of exposed outcrop surfaces determine the current distribution of veneers. Dark-toned rinds several millimeters thick reflect more extensive surface alteration but also indicate combined dust admixture, halite precipitation, and possible minor sulfate removal. Cemented fracture fills that are differentially resistant to erosion occur along the margins of linear fracture systems possibly related to impact. These appear to reflect limited groundwater activity along the margins of fractures, cementing mechanically introduced fill derived principally from outcrop rocks. The limited thickness and spatial distribution of these three features suggest that aqueous activity has been rare and transient or has operated at exceedingly low rates during the protracted interval since outcropping Meridiani strata were exposed on the plains surface.

Citation: Knoll, A. H., et al. (2008), Veneers, rinds, and fracture fills: Relatively late alteration of sedimentary rocks at Meridiani Planum, Mars, *J. Geophys. Res.*, *113*, E06S16, doi:10.1029/2007JE002949.

1. Introduction

[2] Models for the deposition and early diagenesis of outcrop rocks at Meridiani Planum, Mars, invoke liquid water in several discrete events [*Squyres et al.*, 2004, 2006; *Squyres and Knoll*, 2005; *Jolliff and McLennan*, 2006]. In the first instance, the chemical weathering of basaltic precursors to form hydrated sulfates, hematite, and Si-rich phases likely took place under at least episodically aqueous conditions at low pH [*Clark et al.*, 2005; *McLennan et al.*, 2005; *King and McSween*, 2005]. Sulfate-rich sand beds derived from this source and deposited in the Meridiani region show stratigraphic and sedimentological evidence for interactions between a fluctuating water table and eolian processes during deposition, as well as redistribution of grains by surficial water in the upper part of the exposed succession [*Grotzinger et al.*, 2005, 2006]. Cement phases visible in Microscopic Imager (MI) views and bed-specific recrystallization textures apparent in MI and Pancam images attest to early diagenesis in the presence of saturated groundwaters (brines), whereas molds of macroscopic crystals that cut bedding lamination document both precipitation

[1]Department of Organismic and Evolutionary Biology, Harvard University, Cambridge, Massachusetts, USA.
[2]Department of Earth and Planetary Sciences, Washington University, St. Louis, Missouri, USA.
[3]Space Science Institute, Boulder, Colorado, USA.
[4]Department of Astronomy, Cornell University, Ithaca, New York, USA.
[5]Lockheed Martin Corporation, Littleton, Colorado, USA.
[6]Max-Planck-Institut für Chemie, Mainz, Germany.
[7]Department of Physics, University of Guelph, Guelph, Ontario, Canada.
[8]Jet Propulsion Laboratory, California Institute of Technology, Pasadena, California, USA.
[9]Division of Geological and Planetary Sciences, California Institute of Technology, Pasadena, California, USA.
[10]Astrogeology Team, U.S. Geological Survey, Flagstaff, Arizona, USA.
[11]Department of Geosciences, State University of New York, Stony Brook, New York, USA.
[12]NASA Johnson Space Center, Houston, Texas, USA.
[13]Now at Department of Organismic and Evolutionary Biology, Harvard University, Cambridge, Massachusetts, USA.

0148-0227/08/2007JE002949

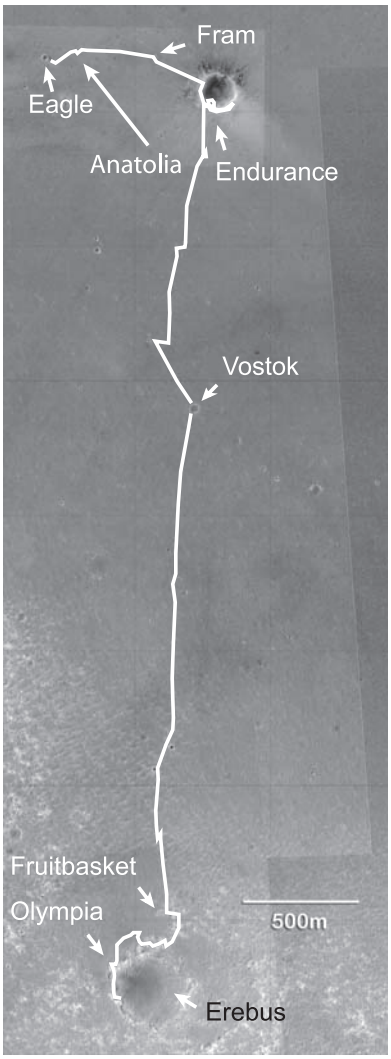

Figure 1. Mars Global Surveyor Mars Orbiter Camera (MOC) cPROTO image showing the portion of the Meridiani plain traversed by Opportunity through sol 733. White line indicates the rover's track. Arrows indicate locations of targets discussed in the text. Image is a downsampled subframe of MOC image R16-02188.

and subsequent dissolution of a diagenetic mineral phase [*McLennan et al.*, 2005]. Spatially overdispersed (distance between adjacent spherules more regular than predicted by random distribution) hematite-rich spherules, themselves commonly surrounded by cements, are interpreted as concretions, providing further evidence for groundwater diagenesis in Meridiani sediments [*McLennan et al.*, 2005].

[3] Throughout the MER mission, the Opportunity rover has encountered additional features that suggest one or more episodes of later diagenetic fluid flow/infiltration of Meridiani sedimentary rocks, as well as surface alteration in possible response to rock-soil-atmosphere interactions. In this paper, we describe three distinct classes of outcrop modification observed at Meridiani. The first, which we call "veneers," consists of thin (submillimeter) coatings that are buff-colored in decorrelation stretches of three color composite images; veneers are common on all rock surfaces and can be removed by abrasion using the Rock Abrasion Tool. The second, referred to as "rinds," comprises much thicker (several millimeters), erosionally resistant and dark-toned zones of surface modification that accumulated on rock surfaces sheltered by a blanket of soil. Rinds cannot be removed by brushing, but where they are thin enough, the Rock Abrasion Tool can abrade through them to expose subjacent unmodified rock. The third, which we call "fracture fills," is a set of erosionally resistant materials that includes a cement component, found along the margins of some fractures within outcrop rock.

[4] For each feature, we describe observable physical and chemical characteristics and constrain timing of emplacement relative to other events recorded by Meridiani outcrops. Sources of information include multispectral data from Pancam [*Bell et al.*, 2003, 2006a], with spectral differences emphasized by decorrelation stretches of three-color composite images [*Bell et al.*, 2004; *Farrand et al.*, 2007]; higher-resolution MI views that document depositional and diagenetic textures [*Herkenhoff et al.*, 2003, 2004]; and chemical and mineralogical analyses by the Alpha Particle X-Ray Spectrometer (APXS) [*Rieder et al.*, 2003] and Mössbauer Spectrometer (MB) [*Klingelhöfer et al.*, 2003] located on Opportunity's instrument arm. Targets span Opportunity's trek from Eagle to Erebus crater, a linear distance of some 4.5 km achieved via a dogleg traverse that totaled 6519 m of wheel odometry in 733 sols (Martian days) of operation (Figure 1).

2. Interpreting Composition From APXS and MB Measurements

[5] Depth of sampling is relevant to the present study because surficial alteration imparts a heterogeneity to outcrop rocks that may be thin enough to impact measurements of different element abundances by APXS. The APXS instrument works by exposing Martian materials to alpha particles and deeper penetrating Pu L shell X rays, both produced by a curium-244 radioactive source [*Rieder et al.*, 2003]. X-ray fluorescence emissions from the sample reveal elements present, with line strengths proportional to element concentrations. The calibration factors used to convert line strengths to elemental abundances are based on calibration with laboratory samples selected for compositional homogeneity. Outcrop rocks on Mars, however, are coated with dust that falls onto surfaces in a quasi-continuous process. Occasional strong winds may remove some of this dust, but MI images and APXS analyses of prebrushed and postbrushed outcrop surfaces usually show that a significant amount of loose material can be removed by brushing without grinding. Martian atmospheric dust particles have been determined to have a mean diameter of 3 μm [*Lemmon et al.*, 2004]. Therefore, for typical soil compositions [*Yen et al.*, 2005], the fluorescent X rays detected by APXS for elements such as Na, Mg, Al, and Si largely originate from a region that is a single dust grain thick. For high-energy X rays, however, such as the 6.4 keV K line from Fe, a 3 μm dust grain is 93% transparent. In this case, Fe stimulated in the substrate provides the main contribution to the Fe signal. Accordingly, measured surface compositions are unlikely to

Table 1. APXS and Mössbauer Compositions Used in Soil and Dusty Soil Average Compositions

	Sol				Average	Sol			Average
	011	026	081	090	Soil	025	060	123	Dust
Feature	Egress		Anatolia				Mont	McDonnell	
Target	Soil Tarmac	Trench Sidewall	Beagle Burrow	Scuff Nougat		Trench Floor	Blanc Les-Hauches	Hill Top Wilson	
				APXS Concentrations (wt %)					
SiO_2	46.3	45.3	47.1	45.6	46.1	45.9	45.3	45.3	45.5
TiO_2	1.04	1.24	1.23	1.09	1.15	1.13	1.02	0.97	1.04
Al_2O_3	9.26	9.05	9.88	9.25	9.36	9.21	9.22	9.21	9.21
Cr_2O_3	0.45	0.46	0.48	0.46	0.46	0.40	0.33	0.36	0.36
Fe_2O_3(T)	20.9	22.1	19.9	20.6	20.9	19.7	19.6	19.5	19.6
MnO	0.37	0.36	0.36	0.38	0.37	0.35	0.34	0.37	0.35
MgO	7.58	7.42	7.59	7.78	7.59	7.49	7.63	7.61	7.58
CaO	7.31	6.72	6.73	6.70	6.87	6.69	6.59	6.73	6.67
Na_2O	1.83	1.92	2.34	2.35	2.11	2.03	2.24	2.38	2.22
K_2O	0.47	0.45	0.41	0.44	0.44	0.49	0.48	0.51	0.49
P_2O5	0.83	0.75	0.74	0.86	0.79	0.80	0.94	0.87	0.87
SO_3	4.99	5.69	4.57	5.81	5.27	6.96	7.34	7.12	7.14
Cl	0.63	0.59	0.49	0.60	0.57	0.70	0.79	0.84	0.77
				APXS Concentrations (*ppm*)					
Ni	423	631	592	456	525	634	470	503	536
Zn	241	348	256	320	291	428	404	376	402
Br	32	130	40	232	109	159	26	35	74
Mössbauer ID	B011SU0 Merlot_Tarmac	B026ST1 Hema-TrenchWall	B078ST1 DogPark_JeffsChoice	B090SD0 PhotoTIDD_Nougat	Average Soil	B025ST2 Hema-Trench	B060SU0 MontBlanc LesHauches	B123SU0 McDonnell	Average Dust
				Mössbauer Phase Assignment (wt % *of Fe*)					
Olivine	39	31	32	27	32	20	28	33	27
Pyroxene	37	35	39	31	36	31	32	36	33
np Ferric Ox	14	22	16	23	19	39	30	19	29
Jarosite	0	0	0	0	0	0	0	0	0
Fe3D3	0	0	0	0	0	0	0	0	0
Magnetite	6	5	7	7	6.3	5	5	8	6.0
Hematite	4	7	6	12	7.3	6	5	4	5.0
$Fe^{3+}/Fe(T)$	0.22	0.32	0.27	0.40	0.30	0.48	0.39	0.28	0.38

reflect simple binary mixing of dust and rock [see also *Goetz et al.*, 2005].

[6] In addition to dust fallout, sand-sized particles and larger clumps can be transported by saltation, deposited on rocks, and trapped in pits and vugs. If soil grains or patches are tens to hundreds of microns thick, then not only the light elements but also higher energy X rays from heavier elements will come mainly from surficial materials and not subjacent rocks or rinds. Even this thicker case does not conform strictly to a simple mixing relationship because the relative intensities of elements depend on the specific composition of the micromatrix in which they are generated.

[7] The MB spectrometer senses more deeply than APXS (200–400 μm for a solid surface and 2–4 mm for porous dusty surfaces versus APXS' $\leq$ 10–50 μm). Thus, it would take 165 μm of typical soil to attenuate the 14.4 keV MB gamma ray by fifty percent [*Morris et al.*, 2006]. On the other hand, MB measurements are more likely than APXS to be affected by a second potentially important source of outcrop heterogeneity, hematite-rich spherules found in Meridiani outcrop rocks. Spherules hidden just beneath the surface would register Fe contents higher than those of spherule-free outcrop lithology.

2.1. Soil and Dust Composition

[8] Soil is widely distributed on the Martian surface, and surficial dust is ubiquitous. Because APXS measurements of veneers, rinds and fracture fills can all be affected by thin coatings of soil or dust, it is important to understand the composition of these constituents. As used in this paper, average soil composition is approximated by the means of analyses on four typical soils [cf. *Yen et al.*, 2005] containing lithic fragments, spherules, and dark sand (sol 011 Tarmac, sol 026 Trench_sidewall, sol 081 Beagle Burrow, and sol 090 Scuff Nougat) and three bright, dust-rich soils (sol 025 Hema_trench, sol 060 Mont Blanc, and sol 123 McDonnell; Table 1). The latter three soils have high concentrations of nanophase ferric oxide and are thus taken to be the most dust-rich soils analyzed at the time of writing [see also *Yen et al.*, 2005; *Morris et al.*, 2006].

[9] The target Mont Blanc_Les Hauches, analyzed along the outer rim of Eagle crater on sol 60, may provide the best representation of dust measured to date by Opportunity. This composition is similar to estimates of global dust chemistry based on in situ measurements by earlier missions [*McSween and Keil*, 2000], remote sensing from orbit [*Hamilton et al.*, 2005], and analyses of dust particles captured by magnets on the MER rovers [*Goetz et al.*, 2005]. Pancam and MI images of Mont Blanc_Les Hauches show that it consists largely of very fine grained material. Its chemical composition as indicated by APXS is roughly similar to those of other Meridiani soils, but S and Cl are about 40% higher; Mössbauer data also indicate significant

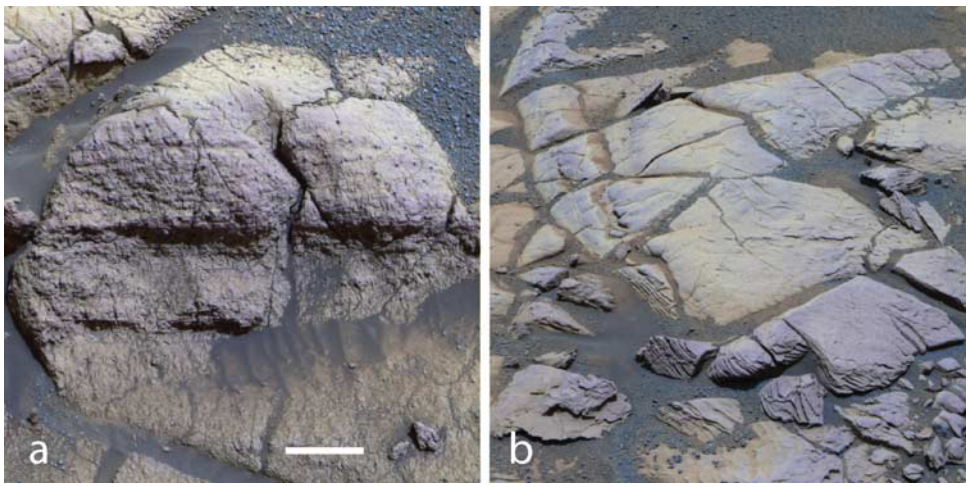

Figure 2. Pancam false color images showing buff veneers and purplish outcrop surfaces. (a) Guadalupe in Eagle crater (sol 27, sequence P2387, false color image acquired using Pancam L2 (753 nm), L5 (535 nm), and L7 (432 nm) filters); (b) Bellemont in outcrop area Olympia (sol 674, sequence P2541, false color image acquired using Pancam L2 (753 nm), L5 (535 nm), and L7 (432 nm) filters). Bar in Figure 2a equals 7 cm for Figure 2a and = 12 cm for Figure 2b. Pancam false color photo credit: D. Savransky and J. Bell (Cornell)/JPL/NASA.

enrichment in nanophase ferric oxide compared to typical Meridiani soil (Table 1).

3. Establishing the Timing of Events

[10] Interpretation of sedimentary features on Mars requires a timeline of events. In the absence of constraining radiometric dates, timelines will be relative; at Meridiani Planum, relevant events include (1) the deposition, diagenesis and surface weathering of strata and (2) subsequent establishment of the regionally extensive cratered surface. Analyses of crater distribution in the Meridiani region indicate that the sedimentary succession examined in situ by Opportunity formed on a Noachian surface and is, in fact, of Late Noachian age, itself [*Hynek et al.*, 2002; *Lane et al.*, 2003; *Arvidson et al.*, 2006]. In contrast, the current sand and granule surface that Opportunity has traversed is only sparsely pocked by small craters, indicating a Late Amazonian surface age [*Lane et al.*, 2003; *Golombek et al.*, 2006], less than 400 Ma in the estimate of *Hartmann and Neukum* [2001]. These constraints allow us to divide events that affected Meridiani outcrops into three broad sets: (1) sediment accumulation and (2) groundwater diagenesis, which predate the establishment and cratering of the current plains surface, and (3) alteration events that postdate formation of the current surface. We focus on the last group in this paper, and collectively refer to these events as late stage alteration.

[11] Relatively recent cratering of the current Meridiani plateau permits further inferences of relative age among late stage events. For example, some veneers have formed on ejecta blocks associated with relatively young craters, requiring formation after cratering. In contrast, rinds on some blocks of outcrop ejecta have orientations that document emplacement before crater formation (see below). Inferences concerning the relative ages of craters on the current plains surface can be drawn from the degree to which persistent sandblasting has beveled ejecta blocks.

4. Buff-Colored Veneers

[12] Approximate true-color Pancam views show various shades of rusty red across the landscape traversed by Opportunity [*Bell et al.*, 2006a, 2006b], but processed and contrast enhanced, visible and near infrared wavelength images reveal a systematic pattern of color differences. (For the remainder of this paper, all descriptions refer to these apparent colors). In these views, most outcrop at Meridiani is tinted either pale buff yellow or purple, with the slight color variations in the rock revealed vividly in decorrelation stretches [*Gillespie et al.*, 1986] of three color composite images, here using Pancam bands L2, 5, and 7 centered at 753, 535, and 432 nm, respectively [see *Farrand et al.*, 2007]. Surfaces with different colors occur in intimate association with each other, but to a first approximation, buff surfaces tend to be flat and low-lying, whereas purplish surfaces commonly protrude above or are oriented at a relatively high angle to local surface topography (Figure 2). These surfaces can also be distinguished using Pancam 11 band spectra. On the basis of slope differences in Pancam's 482 to 535 nm band, *Farrand et al.* [2007] referred to the buff-colored veneers and purplish surfaces as the HFS (High 482 to 535 nm Slope) and LFS (Low 482 to 535 nm Slope) units, respectively.

[13] Opportunity's Rock Abrasion Tool (RAT) [*Gorevan et al.*, 2003] can both whisk away surface dust and grind away outcrop surface, exposing potentially less altered rocks at depths of up to ~10 mm. Buff-colored rock surfaces abraded by the RAT display a different color at depth that ranges from the darker-toned purple characteristic of unabraded LFS, or purple, surfaces to a lighter-toned red. This change in color demonstrates that the buff-colored

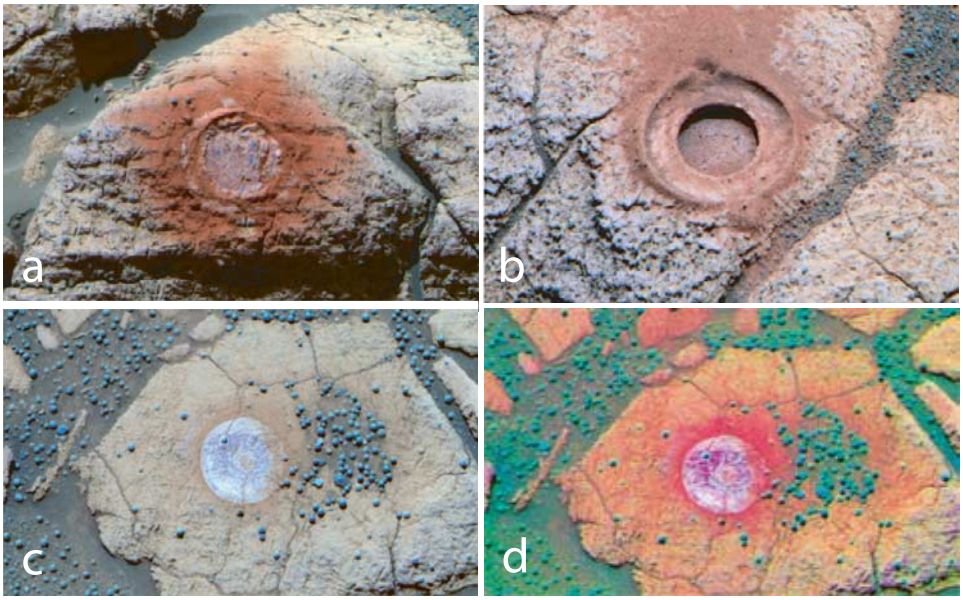

Figure 3. Pancam false color images showing RAT ground outcrop targets. RAT grindings and RAT hole exposures are distinctly redder than the buff surfaces of these outcrops: (a) Guadalupe in Eagle crater (compare with Figure 2a) (sol 37, sequence P2533, false color image acquired using Pancam L2 (753 nm), L5 (535 nm), and L7 (432 nm) filters); (b) Onescoop on outcrop pavement ~200 m north of Erebus crater (sol 574, sequence P2533, false color image acquired using Pancam L2 (753 nm), L5 (535 nm), and L7 (432 nm) filters); (c) Berrybowl in Eagle crater (sol 48, sequence P2568, false color image acquired using Pancam L2 (753 nm), L5 (535 nm), and L7 (432 nm) filters); (d) a decorrelation stretch of the image illustrated in Figure 3c, emphasizing spectral differences among veneers, RAT ground outcrop rock and fine-grained grindings from RAT hole. Pancam false color photo credit: D. Savransky and J. Bell (Cornell)/JPL/NASA.

veneer is an indicator of surface alteration [*Farrand et al.*, 2007]. The veneers are thin, less than a millimeter thick, as inferred from a combination of Pancam features, MI images, and RAT depth estimates (Figures 2 and 3) and confirmed by comparisons of APXS and MB data (see below). Also, they clearly follow the microtopography of surfaces, not bedding. APXS and MB analyses of unaltered, brushed, and abraded targets can, thus, provide information on the chemical nature of surface alteration. To date, Opportunity has performed pregrind and postgrind APXS and MB analyses of nine veneer rock targets, listed in Tables 2 and 3.

4.1. Veneer Chemistry

[14] APXS data indicate that brushed rock surfaces have significantly (Student's t test; $p < 0.05$) higher Si and Al, but about one third less S than ground interiors of the same targets (Tables 2–4). Most brushed rock surfaces also have higher concentrations of the elements Cr, Ti, Na, Ca, and Cl. Concomitant proportional silicate enrichment and sulfate depletion can, in principle, reflect (1) soil and/or dust contamination of surfaces; (2) exterior weathering that preferentially removed physically soft and/or chemically reactive sulfate minerals; or (3) both.

[15] To evaluate the relative importance of weathering alteration versus soil/dust admixture, we consider three cases for which IDD measurements were made on undisturbed, brushed, and ground spots: the targets Escher_Kirchner, Yuri_Gagarin, and Olympia_Ted. In each case, we ask to what extent the composition of brushed and undisturbed surfaces can be understood as a mixture of rock interior composition, obtained from RAT ground surfaces, and soil/dust of average composition.

[16] We first consider Escher_Kirchner, a relatively flat rock located within Endurance crater (Figures 1 and 4). Several locations on the rock Escher were analyzed with the IDD instruments, including targets named Emil Nolde, Kirchner, and Otto Dix. At Kirchner, the undisturbed, veneer-bearing surface was analyzed, then it was brushed with the RAT and reanalyzed, and finally a 7.3 mm deep hole was ground with the RAT. At each stage, the target was measured with the APXS and Mössbauer spectrometer; results are listed in Table 5. As for all measured rock surface-interior pairs, the undisturbed and the brushed surface measurements are significantly lower in S than in corresponding rock interiors −14.3 versus 23 wt % SO_3. Figure 5 shows several representative oxides and elemental concentrations plotted against S, expressed as SO_3, and compared to average compositions of soil and dust.

[17] Several trends can be noted in the plots (Figure 5). First, Al (and Si, not shown) lies along the mixing line between the rock interior and average soil/dust. This is consistent with the hypothesis that veneers record mixing between sulfate-rich sedimentary outcrops and relatively sulfate-poor dust. In contrast, Mg, Fe, and, to a lesser extent, Ca concentrations in both undisturbed surface and brushed surface measurements plot below the rock/soil mixing line, suggesting that simple mixing may not capture

Table 2. APXS and Mössbauer Compositions of Undisturbed (Pre-RAT) Rock Surfaces[a]

	Sol									
	029	030	043	106	142	214	311	400	679	Average
Feature Target	McKittrick pre-RAT	Guadalupe pre-RAT	Flat Rock Mojo_2	LionStone Leo pre-RAT	Kentucky Bluegrass	Escher Kirchner	Pohutu Rk surface	Gagarin as is	Olympia Ted	
				APXS Concentrations (wt %)						
SiO_2	43.1	40.3	43.0	39.7	43.2	41.9	42.6	41.0	40.1	41.6
TiO_2	0.87	0.84	0.88	0.78	0.92	0.81	0.77	0.89	0.85	0.85
Al_2O_3	8.39	7.26	8.39	7.21	7.89	7.81	8.63	7.54	7.29	7.82
Cr_2O_3	0.26	0.17	0.23	0.19	0.24	0.25	0.24	0.20	0.21	0.22
Fe_2O_3(T)	17.4	16.8	17.4	17.0	18.4	16.8	19.2	18.0	18.0	17.7
MnO	0.30	0.30	0.29	0.29	0.24	0.27	0.28	0.34	0.32	0.29
MgO	8.14	7.95	7.82	8.03	8.04	7.67	7.86	7.19	7.27	7.77
CaO	5.72	4.92	5.98	5.11	6.34	5.72	6.33	5.46	5.61	5.69
Na_2O	2.28	1.88	2.26	1.98	0.88	2.63	2.55	2.00	2.04	2.05
K_2O	0.53	0.58	0.56	0.57	0.53	0.59	0.50	0.56	0.57	0.55
P_2O_5	0.97	1.01	0.98	0.98	0.80	1.01	0.91	1.04	1.03	0.97
SO_3	12.7	18.7	13.0	18.8	13.4	14.4	11.1	16.5	17.5	15.1
Cl	0.87	0.87	0.86	1.00	0.83	1.67	0.84	0.98	0.90	0.98
				APXS Concentrations (*ppm*)						
Ni	588	657	633	573	652	435	466	543	571	569
Zn	295	373	414	389	439	352	273	450	541	392
Br	211	43	90	76	139	607	44	73	161	160
Mössbauer Phase Assignment (wt % of Fe)	B029RU0 McKittrick_ AsIs	B030RU0 Guadalupe_ AsIs	B043RU0 FlatRock_ Mojo2	B105RU0 LionStone_ Nala	B142RU0 Kentucky_ BlueGrass2	B213RU0 Escher_ Kirchner	no data	no data	B681RB Olympia Ted	Average
Olivine	10	3	8	0	9	4			1	6
Pyroxene	18	9	17	16	20	16			12	16
npOx	nu	nu	nu	nu	nu	nu			nu	nu
Jarosite	26	27	24	32	21	28			30	26
Fe3D3	16	17	19	21	14	19			18	18
Magnetite	0	0	0	0	0	0				0
Hematite	31	45	32	31	36	32			39	35
Fe^{3+}/Fe(T)	0.72	0.88	0.75	0.84	0.71	0.80			0.87	0.78

[a]Here nu indicates not used in Mössbauer fit.

the full range of surface processes affecting outcrops. Abundances of Ti, Cr, and Mn in brushed and undisturbed rock surfaces are also less than those predicted for a rock/soil mixing line. Last, Na and Cl plot above the mixing line (Figure 5). Other elements that behave similarly include K and P, although these have larger measurement uncertainties than Na and Cl.

[18] Mössbauer data corresponding to the three Escher_Kirchner points add to the story. The undisturbed, brushed, and ground surfaces are very similar in their proportions of Fe-bearing minerals, as indicated by MB spectra (Table 5). All have relatively high jarosite contents, a characteristic of the outcrop lithology, but not of local soils. A plot of the proportions of Fe in pyroxene versus Fe in jarosite illustrates the differences between soil/dust and the different Escher outcrop measurements (Figure 6). Fe in olivine, magnetite, and nanophase ferric oxide versus Fe in jarosite show similar relationships. Olivine and magnetite are present in soil and dust, but not in the sulfate-rich outcrop rock, and except for a small proportion of olivine, they are not seen in MB spectra of rock targets. As noted above, the MB spectrometer senses much deeper than APXS; thus, the combined chemical observations indicate that the surface veneer represented by the APXS chemistry of brushed surfaces must be thin, on the order of tens to $\sim$100 μm [see also *Morris et al.*, 2006]. In the Mössbauer data, olivine appears to be the most sensitive indicator of locally thick soil/dust contamination on the rock surface. For the most part, surface veneer and dust coatings are too thin to contribute significantly to the MB spectra.

[19] The second case we consider is Yuri_Gagarin, located on the Meridiani plain near Vostok crater (Figures 1 and 7). As with Escher_Kirchner, concentrations of Mg, Fe, and Ca in undisturbed and brushed surface spots lie below mixing lines between rock interior and soil/dust (Figure 8). Among minor elements, Cr and Mn have surface concentrations lower than those predicted for a rock/soil mixing line, but Al, Si, and Ti lie along the mixing line. Again, Na, Cl, K, and P all lie above the mixing line, similar to what is seen in the Escher_Kirchner data. For Gagarin, we only have MB data for the abraded rock interior; it is similar to that for Escher_Kirchner. It is worth noting that the undisturbed surface of Gagarin has dust and soil grains on it (as seen in MI images), consistent with the observation (Figure 8) that, for most elements (MgO is the exception), its composition is displaced from the brushed surface composition in the direction of dust and soil compositions, especially in the case of Fe_2O_3(T).

[20] Our third case is the target Ted, located within the "Olympia" outcrop at Erebus crater (Figures 1 and 9). S is depleted in undisturbed and brushed rock surfaces relative to the rock interior; indeed, sulfur depletion is more pronounced in the undisturbed rock, consistent with some dust coating (Table 5). APXS compositional trends for Ted are similar to those of Escher_Kirchner and Gagarin, with the notable exception of MgO (Figure 10). In the Ted APXS

Table 3. APXS and Mössbauer Compositions of Rock Interiors[a]

	Sol									
	031	036	045	108	145	220	312	403	696	Average
Feature Target	McKittrick post-RAT	Guadalupe post-RAT	Flat Rock Mojo2_RAT	Lion Stone post-RAT	Kentucky Cobble Hill2	Escher Kirchner	Wharenhui RAT	Gagarin RAT	Olympia Ted	
					APXS Concentrations (wt %)					
SiO_2	38.3	36.2	36.3	37.2	35.9	36.5	37.5	32.6	34.6	36.1
TiO_2	0.81	0.65	0.74	0.77	0.71	0.75	0.81	0.68	0.71	0.74
Al_2O_3	6.20	5.85	6.18	6.22	5.90	6.06	6.43	4.90	5.40	5.91
Cr_2O_3	0.19	0.17	0.20	0.18	0.18	0.18	0.20	0.17	0.18	0.18
Fe_2O_3(T)	18.4	16.4	17.0	15.9	16.4	17.4	16.7	17.6	17.58	17.0
MnO	0.30	0.30	0.26	0.29	0.33	0.24	0.32	0.35	0.32	0.30
MgO	8.00	8.45	8.38	8.80	9.20	8.37	9.11	7.33	7.08	8.30
CaO	4.42	4.91	5.19	5.03	4.72	5.00	4.10	5.78	5.74	4.99
Na_2O	1.67	1.66	1.64	1.72	1.54	1.63	1.83	1.35	1.51	1.62
K_2O	0.56	0.53	0.59	0.58	0.57	0.57	0.56	0.51	0.55	0.56
P_2O_5	0.99	0.97	1.01	1.01	1.05	1.01	1.08	1.07	1.01	1.02
SO_3	21.3	24.9	23.6	22.8	24.4	23.0	21.3	28.6	26.5	24.1
Cl	0.60	0.50	0.54	0.91	0.65	0.78	1.49	0.61	0.46	0.73
					APXS Concentrations (*ppm*)					
Ni	735	589	656	572	618	564	605	585	537	607
Zn	279	324	427	415	371	314	259	436	554	375
Br	342	30	105	268	54	425	38	54	182	166
Mössbauer phase assignment (wt % of Fe)	B032RR0 McKittrick MiddleRAT	B035RR0 Guadalupe King3	B045RR0 FlatRock Mojo2	B108RR0 LionStone Numma NewNormal	B144RR0 Kentucky CobbleHill	B219RR0 Escher Kirchner	no data	no data	B693RR Olympia Ted	Average
Olivine	1	1	1	1	1	1			2	1
Pyroxene	12	9	15	14	15	15			10	13
npOx	nu	nu	nu	nu	nu	nu			nu	nu
Jarosite	26	38	22	30	28	30			28	29
Fe3D3	22	16	25	22	20	20			20	21
Magnetite	0	0	0	0	0	0				0
Hematite	39	36	38	34	35	35			40	36
$Fe^{3+}/Fe(T)$	0.87	0.9	0.85	0.86	0.84	0.84			0.88	0.86

[a]Here nu indicates not used in Mössbauer fit.

Table 4. Comparison of Rock Exteriors and Rock Interiors

	Rock Exterior									Exterior Divided by Interior		
	McKittrick pre-RAT	Guadalupe pre-RAT	Flat Rock Mojo_2	LionStone Leo preRAT	Kentucky Bluegrass	Escher Kirchner	Pohutu Rk surface	Gagarin As Is	Ted As Is	Average	2 SD	Significant?
Rock interior	McKittrick	Guadalupe	Flat Rock	LionStone	Kentucky	Escher	Wharenhui	Gagarin	Ted			
						APXS (*Exterior/Interior*)						
SiO_2	1.13	1.11	1.19	1.07	1.20	1.15	1.13	1.26	1.16	1.15	0.11	Y
TiO_2	1.08	1.30	1.19	1.01	1.30	1.09	0.95	1.30	1.19	1.16	0.27	N
Al_2O_3	1.35	1.24	1.36	1.16	1.34	1.29	1.34	1.54	1.35	1.33	0.21	Y
Cr_2O_3	1.33	0.99	1.13	1.04	1.32	1.37	1.21	1.17	1.18	1.19	0.26	maybe
Fe_2O_3(T)	0.95	1.02	1.02	1.07	1.12	0.96	1.14	1.02	1.02	1.04	0.13	N
MnO	0.99	0.99	1.14	0.99	0.72	1.10	0.85	0.97	0.99	0.97	0.25	N
MgO	1.02	0.94	0.93	0.91	0.87	0.92	0.86	0.98	1.03	0.94	0.12	N
CaO	1.30	1.00	1.15	1.01	1.34	1.14	1.54	0.94	0.98	1.16	0.40	maybe
Na_2O	1.37	1.14	1.38	1.15	0.57	1.62	1.39	1.48	1.35	1.27	0.60	maybe
K_2O	0.94	1.10	0.94	0.98	0.93	1.03	0.89	1.11	1.03	0.99	0.15	N
P_2O_5	0.98	1.04	0.97	0.97	0.76	1.00	0.84	0.98	1.02	0.95	0.18	N
SO_3	0.60	0.75	0.55	0.82	0.55	0.63	0.52	0.58	0.66	0.63	0.20	Y
Cl	1.45	1.74	1.59	1.09	1.28	2.15	0.56	1.59	1.96	1.49	0.95	maybe
Ni	0.80	1.12	0.96	1.00	1.06	0.77	0.77	0.93	1.06	0.94	0.27	N
Zn	1.05	1.15	0.97	0.94	1.18	1.12	1.06	1.03	0.98	1.05	0.17	N
Br	0.62	1.46	0.86	0.28	2.58	1.43	1.18	1.35	0.88	1.18	1.31	N, variable
						Mössbauer (*Exterior/Interior*)						
Fe in Ol	10	3	8		9	4	no data	no data	0.5	5.8	7.6	Y
Fe in Px	1.5	1.0	1.1	1.1	1.3	1.1	no data	no data	1.2	1.2	0.3	maybe
Fe in Jar	1.0	0.7	1.1	1.1	0.8	0.9	no data	no data	1.1	0.95	0.3	maybe
Fe in Fe3D3	0.7	1.1	0.8	1.0	0.7	1.0	no data	no data	0.9	0.86	0.3	maybe
Fe in Hm	0.8	1.3	0.8	0.9	1.0	0.9	no data	no data	1.0	0.96	0.3	maybe
$Fe^{3+}/Fe(T)$	0.83	0.98	0.88	0.98	0.85	0.95	no data	no data	0.99	0.92	0.1	maybe

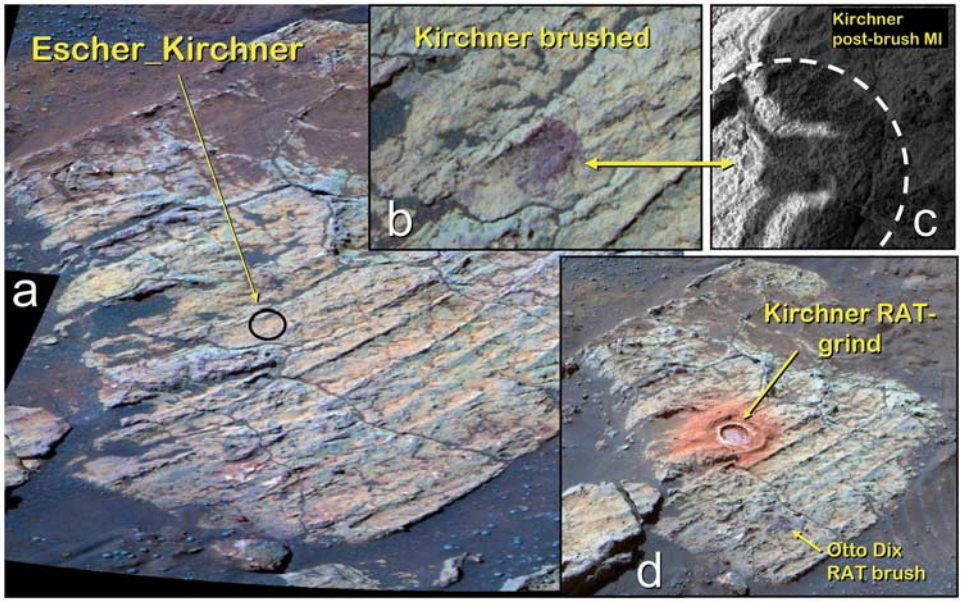

Figure 4. Escher_Kirchner in Endurance crater, chosen to examine compositional differences between outcrop surfaces and interiors exposed by RAT grinding. (a) Pancam false color image of unaltered outcrop surface (sol 208, sequence P2423, false color image acquired using Pancam L2 (753 nm), L5 (535 nm), and L7 (432 nm) filters); (b) Pancam false color image of target after RAT brushing (sol 217, sequence P2576, false color image acquired using Pancam L2 (753 nm), L5 (535 nm), and L7 (432 nm) filters); (c) MI of brushed surface (acquired sol 214, partially in shadow); (d) Pancam false color image of target after RAT grinding, also shown is a second, brushed target called Otto Dix (sol 220, sequence P2582, false color image acquired using Pancam L2 (753 nm), L5 (535 nm), and L7 (432 nm) filters). RAT hole diameter and circle in Figure 4a are 4.5 cm. Pancam false color photo credit: D. Savransky and J. Bell (Cornell)/JPL/NASA; MI credit: NASA/JPL/Cornell/USGS.

set, the Mg concentration of the brushed surface plots along a rock-soil/dust mixing line, whereas Ca and Fe are low relative to the mixing line, as they are in the other two cases (compare Figures 5 and 8). Elements whose compositions in the surface measurements lie along mixing lines between rock interior and soil/dust include Si, Al, Ti, Ni, Zn, and Br. In the case of Ti and Ni, the dust-rich soil composition clearly makes a better mixing component than the typical darker soils. Elements that deviate from soil-rock mixing include Cr, Fe, Ca, Mn (Cr and Fe, and Mn and Ca are nearly identical in their patterns), Na, K (but with large uncertainty), P and Cl. As for other targets, enrichment of NaCl at the surface (undisturbed and brushed) relative to the interior is indicated for Ted.

[21] MI images for the brushed spot on Ted (Figure 9) show some relief and some remaining dust. This residual coating may be thin enough that the low-energy Mg X rays reflect mainly dust, whereas the higher-energy Ca and Fe X rays reflect more of the rock surface (veneer) beneath remaining dust. Cr, which also has a higher energy X-ray line, and which in other samples follows Mg, is also depleted relative to the mixing line (not shown in Figure 9), supporting the possibility that Mg is affected by a thin dust residue. Alternatively, it may just be that, compared to Escher-Kirchner and Gagarin, Ted has an anomalous Mg content.

4.2. Interpretation

[22] To a first approximation, Escher_Kirchner, Gagarin, and Ted all indicate that the observed proportional enrichment of Al and Si and depletion of sulfate in rock surfaces relative to interiors is well explained by surficial dust/soil admixture. Textures observed in MI images suggest that the added materials are predominantly Martian dust and not sandy Meridiani soil per se. As noted above (Figure 6), the essential absence of jarosite from dust, combined with the observation of jarosite in all MB spectra of undisturbed surfaces, requires that buff veneers be thinner than the depth of Mössbauer analyses, i.e., 100–200 μm.

[23] Dust appears to be present to varying degrees on all undisturbed surfaces. Nonetheless, many of the elements measured, especially in the brushed spots, do not lie along mixing lines between rock interiors and soil/dust, indicating that brushed rock surfaces differ in composition from subjacent rock. The enrichment of Na, K, Cl, and P indicates deposition of mineral phases incorporating these elements and reflects some interaction of the rock with moisture at the surface to dissolve and reprecipitate these components. Na and K may combine with Cl to form chlorides that are enriched in the surface veneer. The elevated concentrations of Na and Cl are consistent with enrichments in halite on the order of about 0.5–1.5%. The mineralogical host of P is less clear; however, we note that jarosite (a major sulfate mineralogy in the rocks) may contain some P. If jarosite were to break down chemically at the rock surface and release P, the phosphate could be retained by adsorption onto ferric oxides.

[24] Fe, Mg and Ca in brushed samples generally fall below the mixing line between abraded outcrop rock and

Table 5. APXS and Mössbauer Compositions of Escher_Kirchner, Yuri_Gagarin, and Olympia_Ted IDD Spots[a]

	Sol								
	214	216	220	400	401	403	679	680	696
Feature target Grind depth	Escher Kirchner undisturbed	Escher Kirchner brushed	Escher Kirchner ground (7.26 mm)	Yuri Gagarin undisturbed	Yuri Gagarin brushed	Yuri Gagarin ground (6.0 mm)	Olympia Ted undisturbed	Olympia Ted brushed	Olympia Ted ground (2.7 mm)
				APXS Concentrations (wt %)					
SiO_2	41.9	41.5	36.5	41.0	38.3	32.6	40.1	38.2	34.6
TiO_2	0.81	0.79	0.75	0.89	0.78	0.68	0.85	0.78	0.71
Al_2O_3	7.81	7.59	6.06	7.54	6.71	4.90	7.29	6.69	5.40
Cr_2O_3	0.25	0.21	0.18	0.20	0.17	0.17	0.21	0.19	0.18
Fe_2O_3(T)	16.8	16.5	17.4	18.0	16.9	17.6	18.0	17.8	17.6
MnO	0.27	0.28	0.24	0.34	0.31	0.35	0.32	0.31	0.32
MgO	7.67	7.57	8.37	7.19	7.25	7.33	7.27	7.23	7.08
CaO	5.72	5.66	5.00	5.46	5.36	5.78	5.61	5.45	5.74
Na_2O	2.63	2.46	1.63	2.00	1.79	1.35	2.04	1.93	1.51
K_2O	0.59	0.61	0.57	0.56	0.57	0.51	0.57	0.58	0.55
$P2O_5$	1.01	1.00	1.01	1.04	1.03	1.07	1.03	1.03	1.01
SO_3	14.4	15.6	23.0	16.5	21.5	28.6	17.5	20.6	26.5
Cl	1.67	1.72	0.78	0.98	0.92	0.61	0.90	0.80	0.46
				APXS Concentrations (*ppm*)					
Ni	435	449	564	543	574	585	571	548	537
Zn	352	287	314	450	405	436	541	536	554
Br	607	608	425	73	67	54	161	177	182
Mössbauer Phase Assignment (wt % of Fe)	B213RU0 Escher_Kirchner Undisturbed	B215RB0 Escher_Kirchner Brushed	B219RR0 Escher_Kirchner Ground			B404RR0 Yuri_Gagarin Ground	B681RB Olympia Ted		B693RR Olympia Ted
Olivine	4	1	1	no data	no data	1	1	no data	2
Pyroxene	16	15	15	no data	no data	7	12	no data	10
npOx	nu	nu	nu	no data	no data	nu	nu	no data	nu
Jarosite	28	29	30	no data	no data	32	30	no data	28
Fe3D3	19	21	20	no data	no data	24	18	no data	20
Magnetite	0	0	0	no data	no data	0	0	no data	0
Hematite	32	33	35	no data	no data	37	39	no data	40
Olivine/Pyroxene	0.25	0.07	0.07	no data	no data	0.14	0.08	no data	0.20
Fe^{3+}/FeT	0.80	0.84	0.84	no data	no data	0.92	0.87	no data	0.88

[a]Here nu indicates not used in Mössbauer fit.

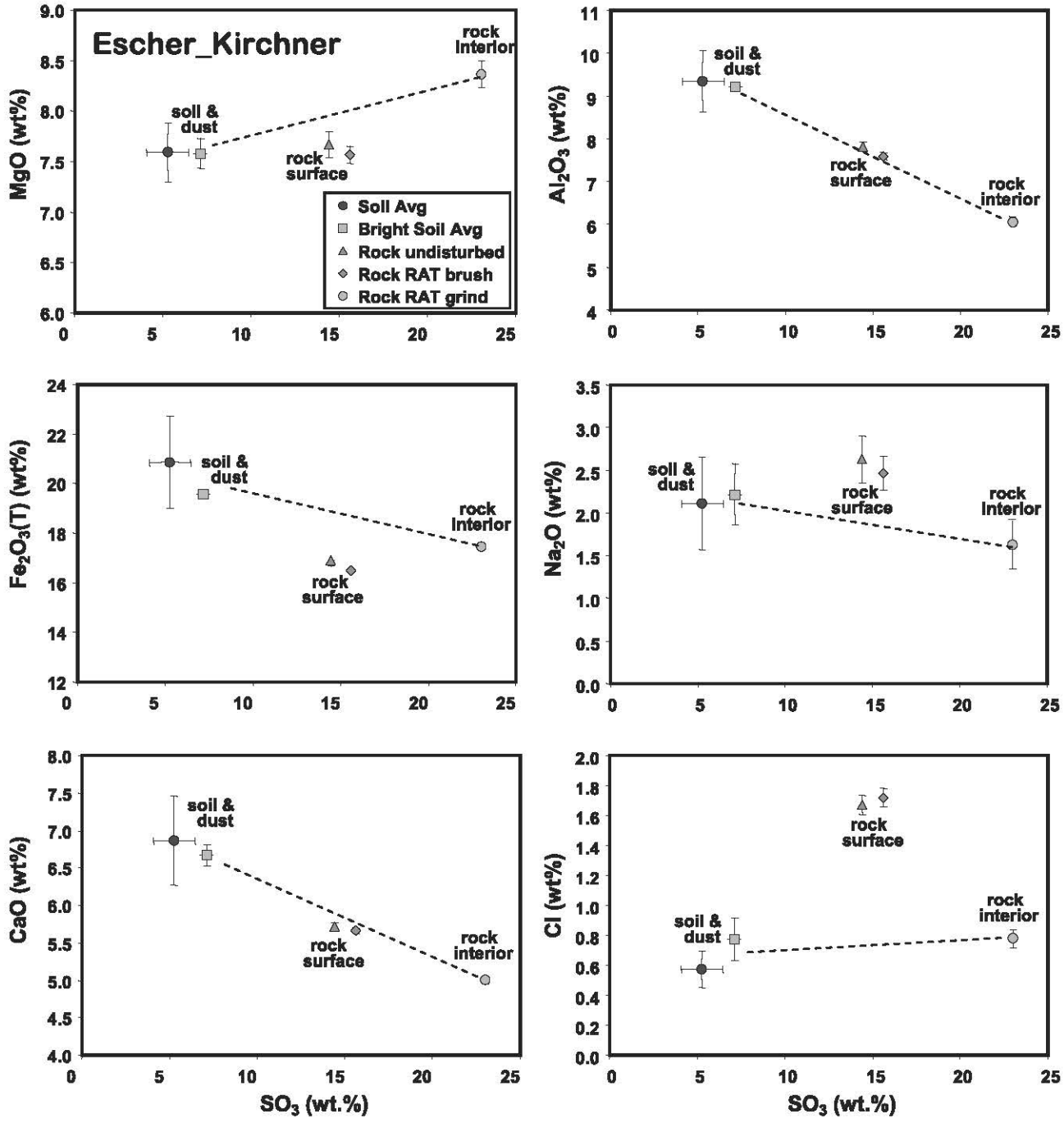

Figure 5. Escher_Kirchner: APXS composition of unaltered outcrop surface, brushed surface, and rock interior exposed by RAT grinding, compared with composition of regional soil/dust. The *x* axis for all graphs is weight percent SO_3; the *y* axis shows weight percent abundance of selected other components; dashed lines indicate a linear mixing line between rock interior and soil/dust.

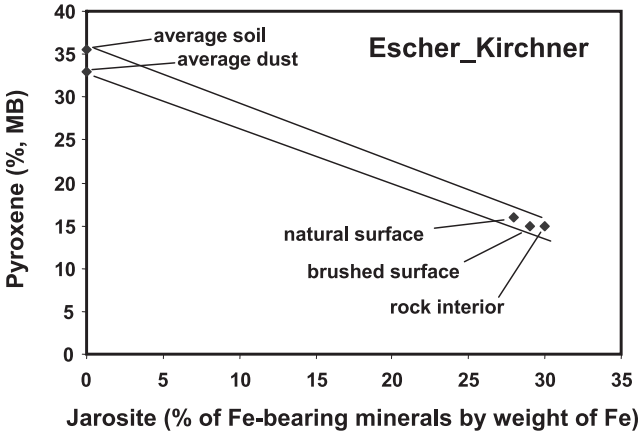

Figure 6. Escher_Kirchner; plot showing proportional abundance of jarosite versus pyroxene (weight percent of Fe apportioned to each mineral) for rock interior, brushed surface, unaltered surface and regional soil/dust, as determined by MB. Lines indicate the mixing trend between rock interior and jarosite-free soil/dust.

soil, and a reading of the data that neglects the variable depth sensitivity of the APXS technique would suggest that Fe-, Ca-, and Mg-sulfates are slightly and variably depleted in veneers. We can eliminate the end-member hypothesis that rock surface-interior differences simply reflect selective loss of sulfate minerals; differences in Mg, Ca, and Fe contents measured for brushed versus ground samples are much too small to account for the observed 30% S loss by sulfate removal. Nonetheless, if APXS data faithfully record the composition of the veneers, at least minor (~3 wt %) loss of sulfate minerals by differential dissolution, abrasion by sand blasting, or both is required (Figure 11).

[25] APXS measurements are consistent among samples, but the caveats about APXS analysis of heterogeneous materials, outlined in a previous section, need to be considered here. Because the absorption of X rays varies as a function of X-ray energy, which is essentially proportional to atomic number, the measured concentrations of lighter elements will differentially reflect the composition of any thin veneer of dust, while those of heavier elements will tilt toward substrate composition. Observed compositional variations in undisturbed and brushed outcrop surfaces compared to linear rock-soil/dust mixing could reflect differential X-ray absorption through dust coatings. To test this possibility, we model the effects of differential absorption with a nonlinear mixing model as described next.

[26] Using "transmission factors" calculated from average attenuation cross sections for the characteristic X-ray lines of measured elements, taken from *Gellert et al.* [2006, Table 1], we can model the composition that would be measured by the APXS if the target consisted of a substrate of outcrop rock and a thin coating of Meridiani dust [*Jolliff et al.*, 2007]. Using the case of Escher_Kirchner as an example, and the average composition of three bright soils as an approximation of the composition of dust, we find that thicknesses equivalent to 0.5–0.9 mg/cm^2 would produce about the same "apparent" depletion of SO_3 relative to the interior rock composition as was measured on the natural (undisturbed) surface and the brushed surface (Figure 12). These coating thicknesses would correspond to 5–9 μm if the bulk density of the coating were 1 g/cm^3. For other elements whose concentrations are modeled in this way, the sense of variation relative to a linear rock-soil mixing line is the same as for the measured concentrations, suggesting that this effect may play a role; however, the deviations are not quantitatively matched by the nonlinear model compositions, leaving open the possibility of sulfate loss at the exposed rock surface. In the case of Escher_Kirchner (Figure 12), the nonlinear absorption model appears to be promising for Mg and possibly Fe; however, the model overpredicts variations in Ca and Al and significantly underpredicts variations in Cl and Na.

[27] The APXS data modeled according to expected X-ray transmission through a thin dust coating, thus, provides bounds on probable composition. At most, sulfate loss is a few percent; much of the variation in composition between rock interiors and rock surfaces can be accounted

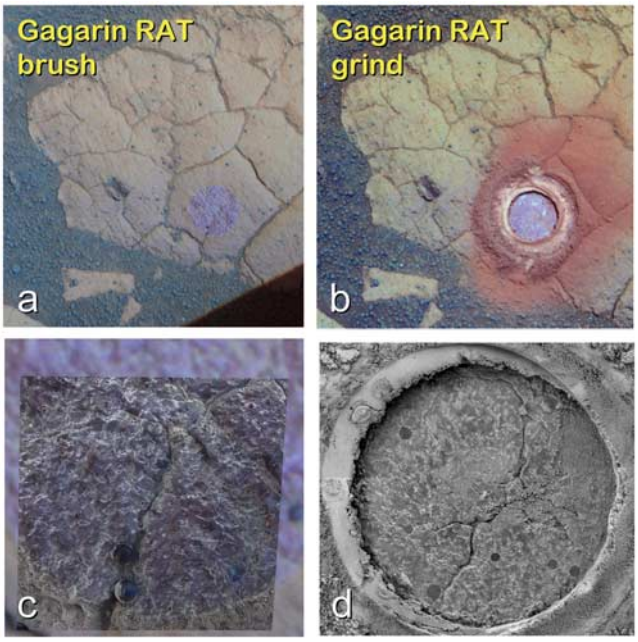

Figure 7. Images of rock target Gagarin, located just north of the crater dubbed Vostok. (a) Pancam false color image following RAT brushing (sol 401, sequence P2570, false color image acquired using Pancam L2 (753 nm), L5 (535 nm), and L7 (432 nm) filters); (b) following RAT grinding (sol 405, sequence P2578, false color image acquired using Pancam L2 (753 nm), L5 (535 nm), and L7 (432 nm) filters); (c) MI image merged with Pancam false color showing lower part of the brushed area, the spherule along the lower edge can be seen in both the MI and Pancam images; (d) MI mosaic of rock interior exposed by RAT grinding, acquired on sol 403 when target was in shadow. RAT hole diameter is 4.5 cm; grind depth is ~6 mm. Pancam false color photo credit: D. Savransky and J. Bell (Cornell)/JPL/NASA; MI credit: NASA/JPL/Cornell/USGS.

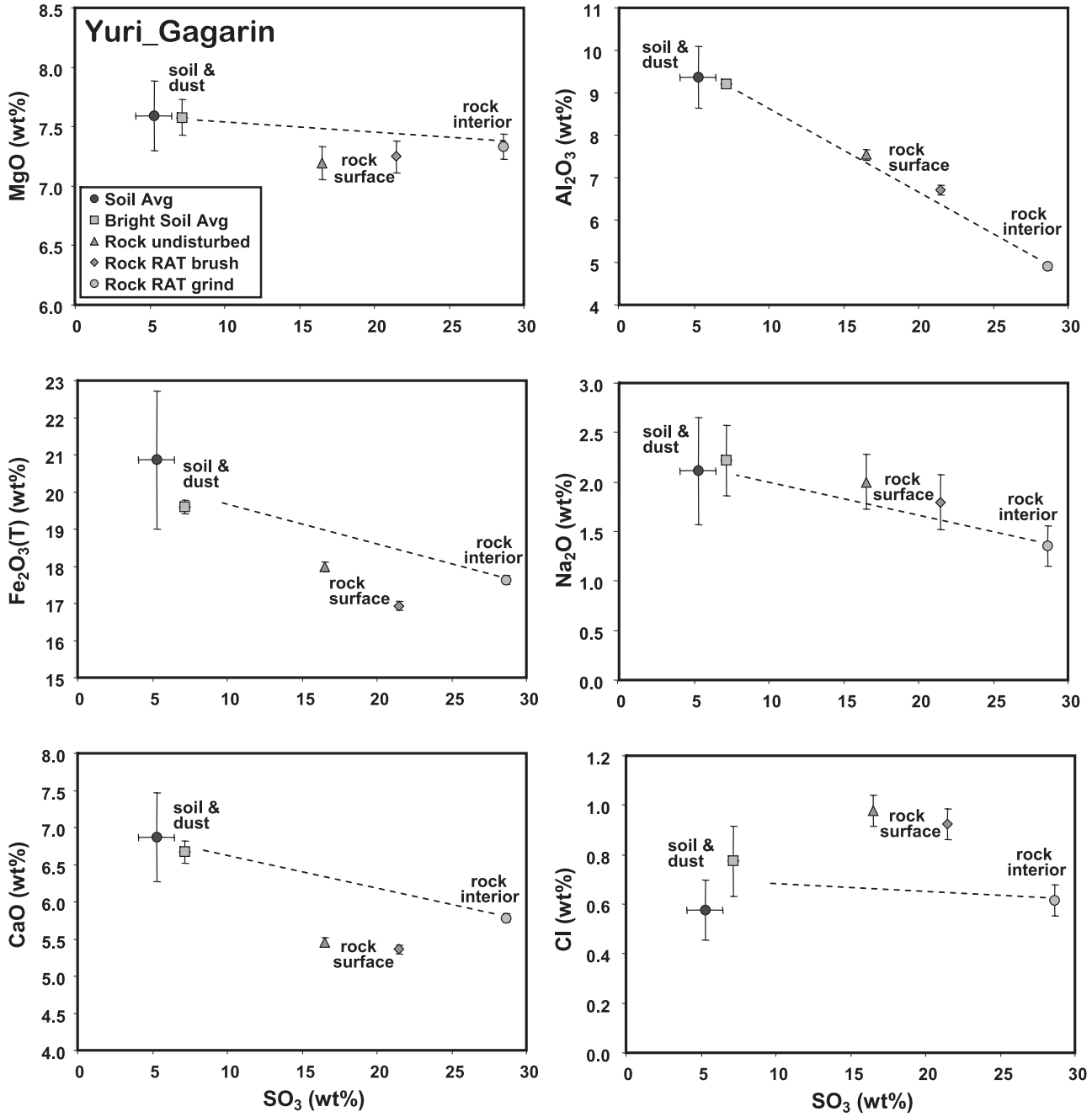

Figure 8. Yuri_Gagarin: APXS composition of unaltered outcrop surface, brushed surface, and rock interior exposed by RAT grinding, compared with composition of regional soil/dust. The *x* axis for all plots is weight percent SO_3; the *y* axis shows weight percent abundance of selected other components; dashed lines indicate a linear mixing line between rock interior and soil/dust.

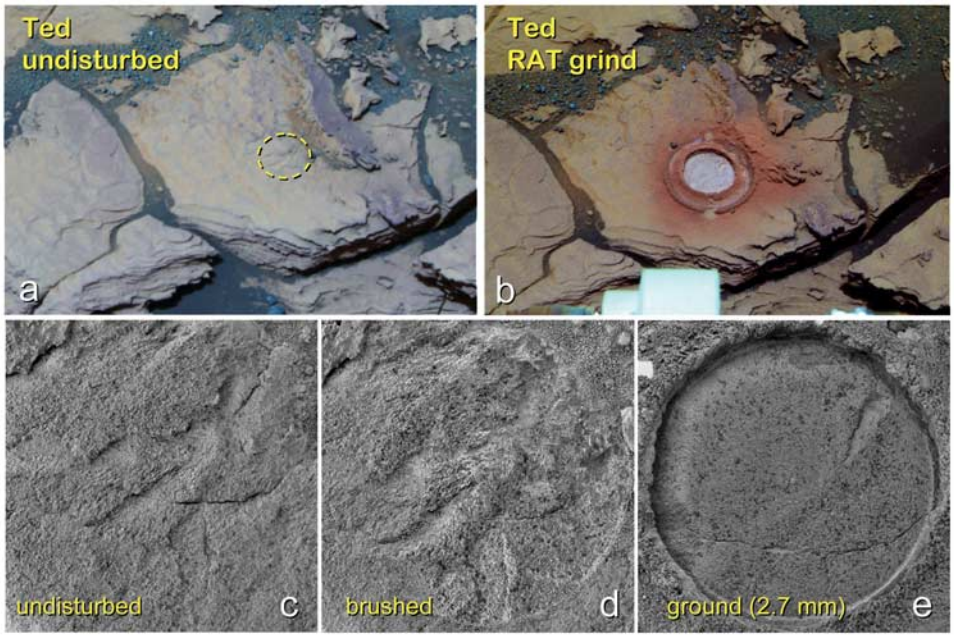

Figure 9. Images of the rock target Ted located on the Olympia outcrop along the northwestern rim of Erebus crater. (a) Undisturbed surface showing buff veneer on rock surface (sol 663, sequence P2294, false color image acquired using Pancam L2 (753 nm), L5 (535 nm), and L7 (432 nm) filters); (b) target after RAT grind (sol 691, sequence P2567, false color image acquired using Pancam L2 (753 nm), L5 (535 nm), and L7 (432 nm) filters); (c–e) MI mosaics of unaltered rock surface (sol 679), brushed surface (sol 684), and interior exposed by RAT grinding to a depth of 2.72 mm (sol 691). RAT hole diameter is 4.5 cm. MI images taken while target was in shadow (credit NASA/JPL/Cornell/USGS). Pancam false color photo credit: D. Savransky and J. Bell (Cornell)/JPL/NASA.

for by some combination of linear and nonlinear mixing with dust or soil grains on the exterior surfaces.

4.3. Processes and Timing

[28] In summary, then, chemical and mineralogical analyses of buff veneers and subjacent portions of the same outcrop rocks indicate that veneers reflect a combination of dust admixture and halite (and possibly other minor components) precipitation, with possible limited loss of sulfate minerals. The proportional effects of these processes cannot be ascertained from available data (i.e., there is no unique solution), but one cannot escape the conclusion that the total amount of alteration by the three processes combined is small.

[29] Veneers occur on exposed portions of the current Meridiani plains surface and on reoriented blocks within craters, including crater wall and ejecta blocks at Fram, among the freshest craters encountered to date by Opportunity (Figures 1 and 11). Veneers coat surfaces that contain textures modified by recrystallization, hematite-rich spherules weathering out of outcrop rocks, and three-dimensional crack systems that form polygons in surface view. Thus, the formation of buff veneers postdates not only the depositional and diagenetic events discussed in previous papers by the MER team [e.g., *McLennan et al.*, 2005], but also cratering, the erosional development of current regional topography, and, in many cases, formation of polygonal crack systems. The buff veneer tends to be absent where sandblasting is most effective, hence the apparent purplish tint that dominates emergent and vertically oriented rock surfaces. Some color variation is also intrinsic to different sedimentary strata [*Farrand et al.*, 2007]. Therefore, color of rock surfaces reflects deposition and early diagenesis as well as their subsequent history of surface exposure and modification.

[30] We hypothesize that thin films of water form transiently under favorable environmental conditions at rock surfaces. These films persist longest (and therefore have maximal geochemical effect) where the outcrop surface is blanketed by soil. The thin water layer is hypothesized to dissolve minute quantities of soluble salts and then reprecipitate them at the outcrop surface. Deposits include NaCl, perhaps KCl, and some form of phosphate or phosphorous adsorbed onto ferric oxides. Chlorides might also be leached from soil or dust and then precipitated on the outcrop surface from a saturated film of water.

[31] Local exposure leaves surfaces vulnerable to wind erosion and, probably, continuing surficial alteration. The rates of both processes may vary with obliquity-driven climate variations. Thus, the current patchy distribution of buff and purple surfaces probably reflects a continuing dynamic balance between chemical alteration and wind erosion at Meridiani, with one process or the other dominating locally depending on the extent of exposure to saltating sand grains.

[32] One might wonder whether Meridiani outcrops have been pervasively altered by late diagenetic events to depths exceeding the sample depths even of RAT grinds. Would the

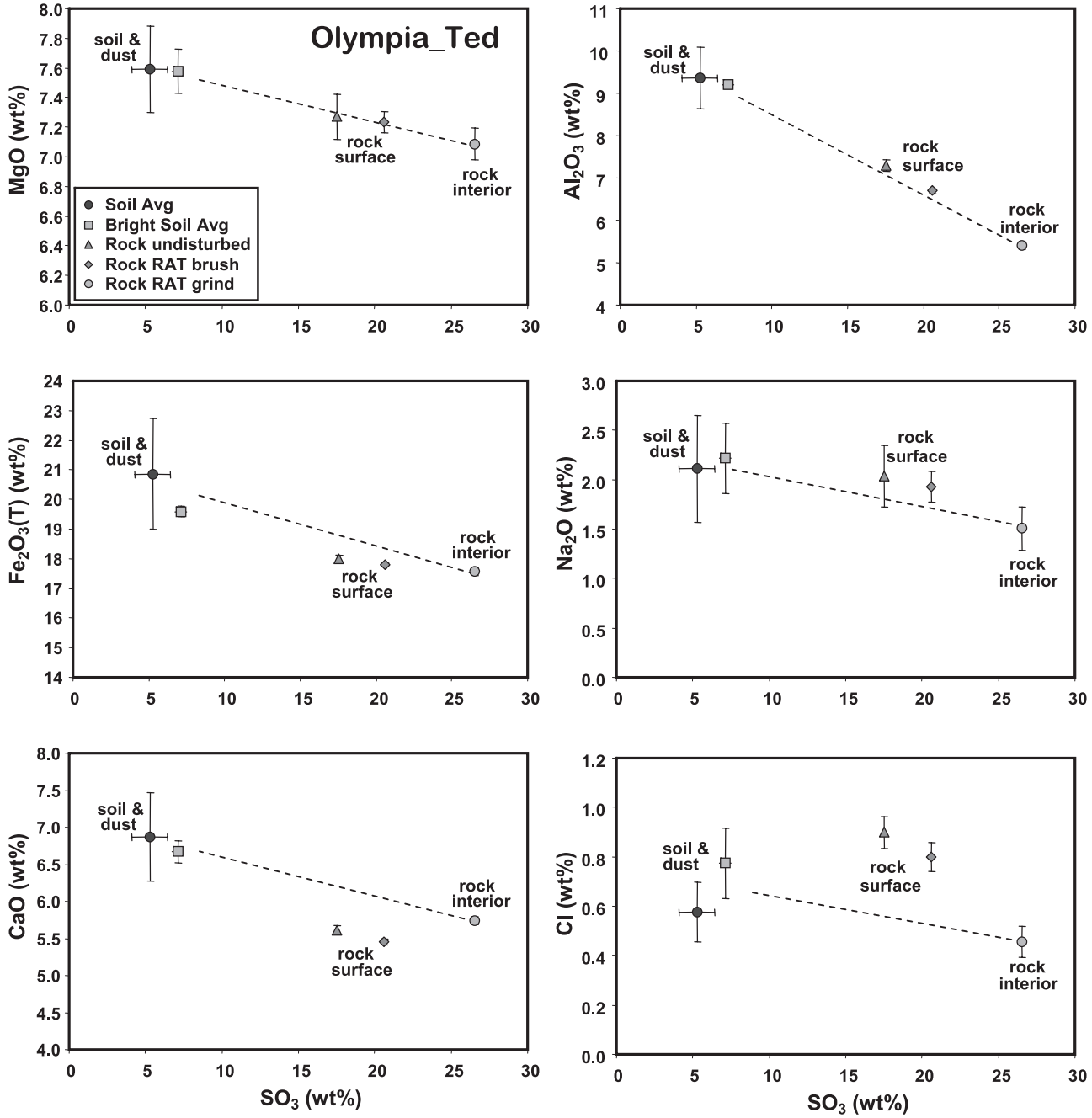

Figure 10. Olympia_Ted: APXS composition of unaltered outcrop surface, brushed surface, and rock interior exposed by RAT grinding, compared with composition of regional soil/dust. The *x* axis for all plots is weight percent SO_3; the *y* axis shows weight percent abundance of selected other components; dashed lines indicate a linear mixing line between rock interior and soil/dust.

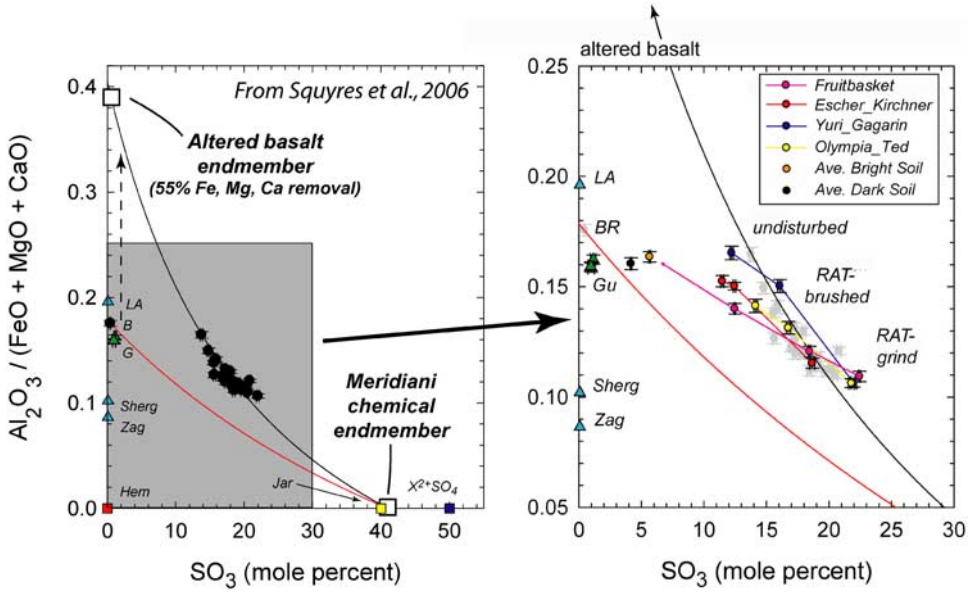

Figure 11. Plot of molar $Al_2O_3/(FeO_T + MgO + CaO)$ versus SO_3 (mole percent). Variation in the *y* axis on this diagram is largely controlled by chemical weathering, as the sum of divalent cations (Fe^{2+}, Mg, and Ca) decreases in the residual basalt relative to Al^{3+}. The black mixing line represents mixing between the inferred and identified chemical components of RAT ground Meridiani outcrop material and a chemically weathered basalt composition with 55% FeO_T + MgO + CaO removed. Inferred and identified chemical components include jarosite, hematite, Fe3D3 component (with abundances constrained by Mössbauer), and Mg- and Ca-sulfates (with abundances estimated from mixing relationships). Constraints on the abundances of chemical components are discussed in detail by *McLennan et al.* [2005]. The black line closely fits the chemical variation of RAT ground Meridiani outcrop material on this diagram (shown by inset and light gray points), as discussed by *Squyres et al.* [2006]. APXS analyses (undisturbed, brushed and RAT ground) for Fruit Basket, Escher, Gagarin, and Ted plotted on this diagram suggest that two processes influence the chemical composition in these samples: sulfate loss and soil addition. Sulfate loss is indicated by a trend observed in all RAT ground, brushed and undisturbed samples that moves from the ''chemical end-member'' to the ''siliciclastic end-member'' (i.e., generally following the black mixing line). Soil addition is shown by the position of brushed and undisturbed materials relative to RAT ground materials; the materials affected by soil addition plot off of the black mixing line toward a composition closer to that of the average soil analyses (shown by black and orange points). Other basaltic compositions plotted for reference are Los Angeles meteorite (LA), Bounce rock (BR), Adirondack and Humphrey (Gu), Shergotty meteorite (Sherg), and Zagami meteorite (Zag).

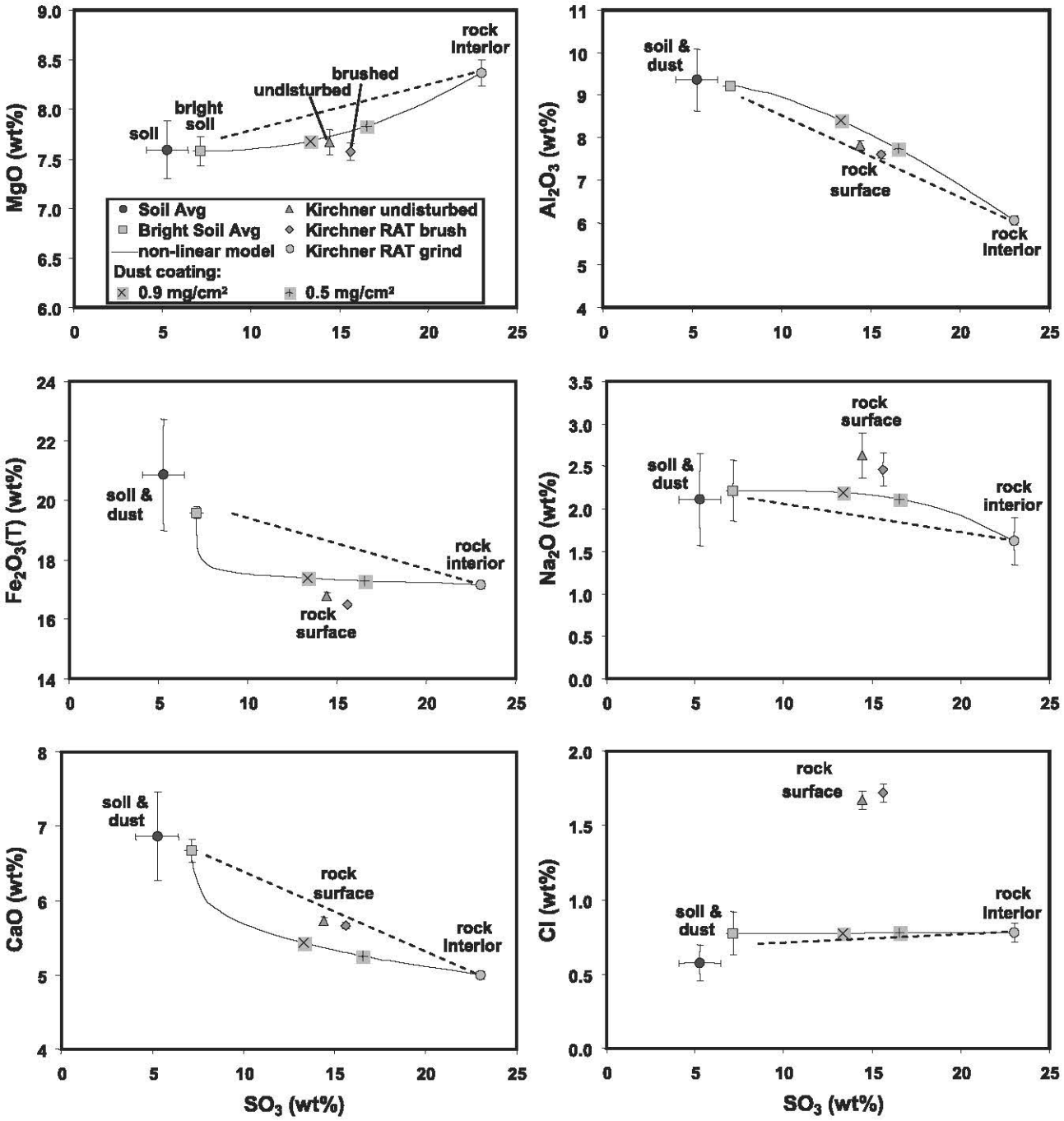

Figure 12. Escher_Kirchner APXS compositions of unaltered outcrop surface, brushed surface, and rock interior exposed by RAT grinding, compared with composition of regional soil/dust, as in Figure 5. The pluses and crosses indicate model predictions for expected abundance measurements if APXS values reflect the differential penetration of X rays through dust coatings of 0.5 mg/cm^2 (pluses) and 0.9 mg/cm^2 (crosses) thicknesses. See text for further discussion.

Figure 13. Rock rinds at Fram crater (sol 87, sequence P2534, false color image acquired using Pancam L2 (753 nm), L5 (535 nm), and L7 (432 nm) filters). Arrows mark possible "case-hardened" surfaces that form overhangs shadowing softer, more readily eroded rock. The inclined orientations of these features indicate that they existed prior to the formation of this relatively fresh crater. Field of view at rock distance approximately 2 m. Pancam false color photo credit: D. Savransky and J. Bell (Cornell)/JPL/NASA.

presence of such alteration be recognizable, given available data? Regional compositional similarities among all sampled outcrop rocks at Opportunity's landing site are notable. However, compositional variations correspond to stratigraphic position of samples [*Clark et al.*, 2005], and the presence, absence, and if present, size and abundance of hematite-rich spherules also varies with stratigraphic position [*Squyres et al.*, 2006]. These observations, coupled the absence of pervasive alteration textures in MI images [*McLennan et al.*, 2005] lend no support to a hypothesis that all rocks sampled at all depths have been pervasively altered by penetrative diagenesis that took place after the current plains surface was established.

5. Rinds

[33] Rinds on Meridiani outcrop rocks differ from veneers in thickness, color, texture, and resistance to erosion. The rinds (Figures 13–16) are dark-toned features, ~2–8 mm thick, that form conspicuous coatings on outcrop rocks across the Meridiani plains. First observed at Shoemaker's Patio, within Eagle crater, the rinds also have been noted along the Anatolia fracture system east of Eagle crater, within or around Fram and Endurance craters, on outcrop pavements exposed along the traverse south of Endurance (especially multiple exposures just north of Erebus crater), and in exposures at Olympia, near the northwestern margin of Erebus crater (Figure 1). The most informative APXS and MB data for this class of feature, however, come from the paired rind/subjacent outcrop targets Lemon Rind and Strawberry near Erebus crater (Figures 1 and 16 and Table 6).

[34] Two observations indicate that the rinds are alteration features rather than distinct sedimentary units. First, at Shoemaker's Patio, Pancam images of reoriented outcrop blocks show that obliquely oriented bedding lamination is continuous between outcrop and rind (Figure 14c). Also, Pancam and MI images show that rinds contain some of the same textural elements found in subjacent outcrops–

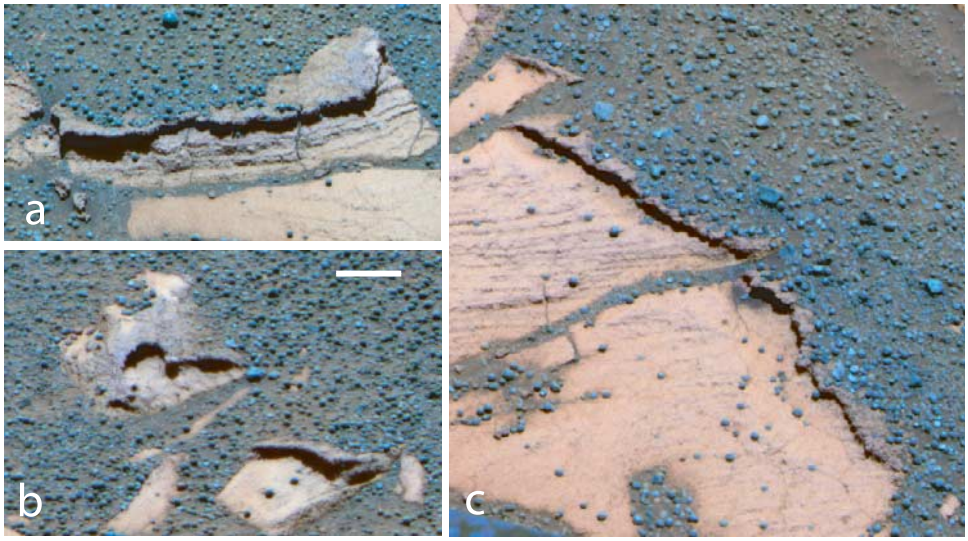

Figure 14. Pancam false color images of rock rinds at Shoemaker's Patio in Eagle crater. (a) Sol 50, sequence P2578, false color image acquired using Pancam L2 (753 nm), L5 (535 nm), and L7 (432 nm) filters; (b) sol 50, sequence P2579, false color image acquired using Pancam L2 (753 nm), L5 (535 nm), and L7 (432 nm) filters; (c) sol 50, sequence P2576, false color image acquired using Pancam L2 (753 nm), L5 (535 nm), and L7 (432 nm) filters. Bar equals about 3 cm in all images. Pancam false color photo credit: D. Savransky and J. Bell (Cornell)/JPL/NASA.

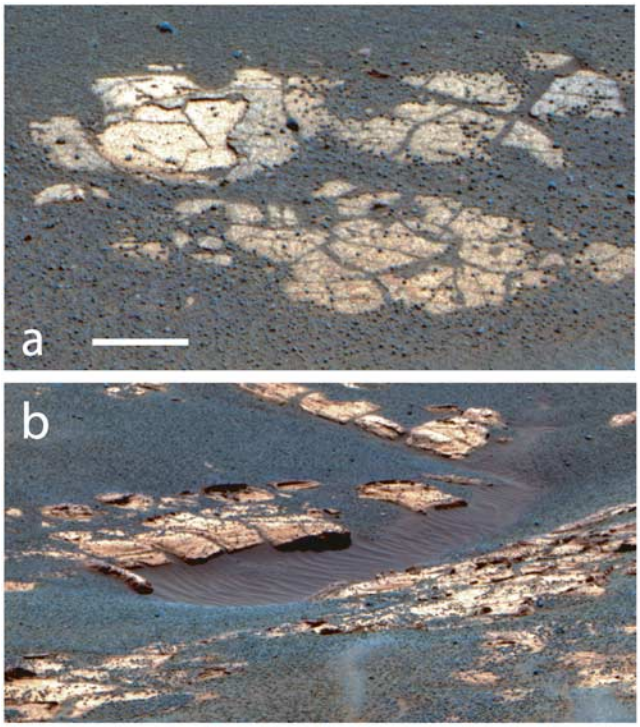

Figure 15. Pancam false color images of rock rinds at target Bookcover, in the Fruit Basket region just north of Erebus crater (Figure 15a) and Anatolia (Figure 15b). (a) Sol 580, sequence P2540, false color image acquired using Pancam L2 (753 nm), L5 (535 nm), and L7 (432 nm) filters; (b) sol 74, sequence P2591, false color image acquired using Pancam L2 (753 nm), L5 (535 nm), and L7 (432 nm) filters. Bar in Figure 15b approximately 10 cm for Figure 15a and 90 cm for Figure 15b. Pancam false color photo credit: D. Savransky and J. Bell (Cornell)/JPL/NASA.

hematite spherules in several examples (e.g., Figure 14b) and tabular crystals in the target Lemon Rind (Figure 16b). The latter, at least, cannot be reworked outcrop material; tabular crystals are recorded as molds in unaltered outcrop, but in rinds, they are filled structures that weather into positive relief. The Lemon Rind surface also displays apparently cubic features that could be molds of later diagenetic halite (Figure 16b) [*Yen et al.*, 2006; *Squyres et al.*, 2006].

[35] Decorrelation stretches of three-color Pancam images and examination of 11-point Pancam spectra emphasize that rinds are spectrally distinct from underlying outcrop rocks [*Farrand et al.*, 2007]. The darker tone and concave-upward NIR spectra of rinds is consistent with the presence of some ferrous or ferric iron phase with an absorption minimum at or near 900 nm.

[36] The chemistry of rind material and its relationship to underlying bedrock was characterized best at Lemon Rind/Strawberry. The Lemon Rind measurement was performed on rind material that was abraded with the RAT to a depth of ~1.5 mm. This abrasion depth was chosen to be deep enough to remove any veneer, but shallow enough to avoid penetration of subjacent rock. The Strawberry target was abraded to a depth of ~8 mm, penetrating deeply into the outcrop rock on which the rind was developed. MI images of Lemon Rind show that grinding was incomplete; therefore, postgrind data for Lemon Rind are conservatively interpreted as a mixture of surface and subsurface rind material.

[37] The chemistry of the rind (Lemon Rind) shows a close relationship to the composition of the subjacent rock (Strawberry), but differs as follows: (1) a 7–8 wt % (relative) increase in SiO_2 and Al_2O_3, (2) a 16 wt % (relative) decrease in SO_3, (3) a slight (3 wt %) decrease in MgO and increase (1–2wt %) in Fe_2O_3 and CaO, and (4) a ~30–40 wt % enrichment of Na_2O and > 100 wt % increase in Cl in a nearly 1:1 molar ratio with Na (Table 6).

[38] We can also consider the compositional variations observed in the rind in terms of deviations from mixing lines between rock interior and soil/dust, as we did for the three cases described in section 2 above (Figure 17). Measurements of Lemon Rind include one made after a

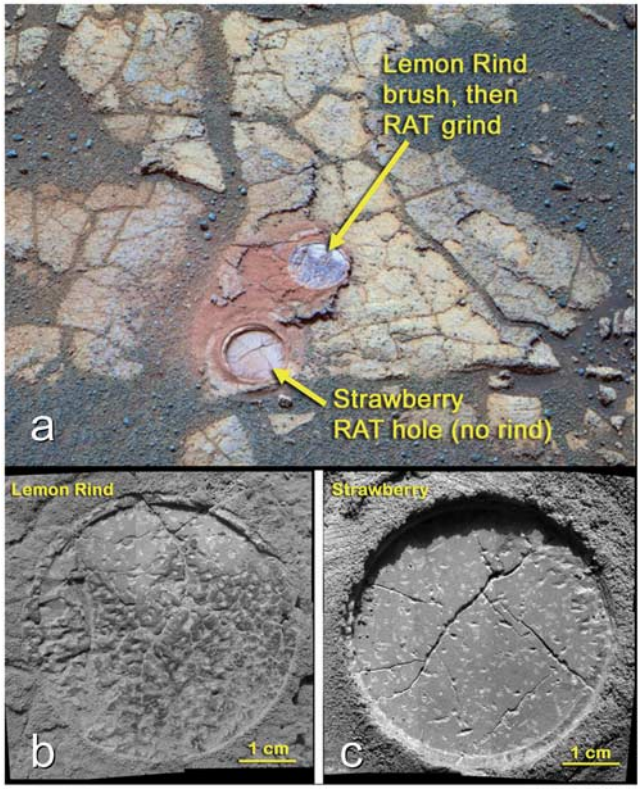

Figure 16. Pancam false color images of rock rind and subjacent outcrop rock at Fruit Basket, showing (a) RAT Ted IDD targets Lemon Rind (a rind) and Strawberry (subjacent outcrop rock) (sol 561, sequence P2591, false color image acquired using Pancam L2 (753 nm), L5 (535 nm), and L7 (432 nm) filters); (b and c) MI mosaics of RAT ground surfaces of Lemon Rind (sol 560) and Strawberry (sol 558), respectively. RAT hole diameter is 4.5 cm, illumination from top. MI credit: NASA/JPL/Cornell/USGS. Pancam false color photo credit: D. Savransky and J. Bell (Cornell)/JPL/NASA.

Table 6. APXS and Mössbauer Compositions of the Fruit Basket IDD Spots (Lemon Rind and Strawberry)[a]

	Sol		
	B556	B560	B558
Feature target	Fruit Basket Lemon Rind brushed	Fruit Basket Lemon Rind ground (1.5 mm)	Fruit Basket Strawberry ground (~3 mm)
	APXS Concentrations (wt %)		
SiO_2	40.2	35.1	32.8
TiO_2	0.89	0.75	0.72
Al_2O_3	7.49	6.17	5.72
Cr_2O_3	0.24	0.19	0.19
Fe_2O_3(T)	18.8	17.8	17.6
MnO	0.37	0.38	0.39
MgO	7.07	7.83	8.09
CaO	6.07	5.20	5.13
Na_2O	2.22	2.02	1.57
K_2O	0.55	0.54	0.50
$P2O_5$	1.07	1.05	0.99
SO_3	15.3	23.1	27.4
Cl	1.49	1.54	0.57
	APXS Concentrations (*ppm*)		
Ni	525	508	504
Zn	474	457	563
Br	67	67	84
Mössbauer phase assignment (wt % of Fe)	B557RB0 Fruit-Basket_Lemon Rind brushed	B560	B558
Olivine	6	no data	no data
Pyroxene	13	no data	no data
npOx	nu	no data	no data
Jarosite	33	no data	no data
Fe3D3	18	no data	no data
Magnetite	0	no data	no data
Hematite	30	no data	no data
Olivine/ Pyroxene	0.46	no data	no data
Fe^{3+}/FeT	0.81	no data	no data

[a]Here nu indicates not used in Mössbauer fit.

RAT brushing as well as the one made after the 1.5 mm grind.

[39] Many of the compositional trends follow similar patterns to the veneers. The concentration of S is not as low in the abraded Lemon Rind as it is in the brushed veneers (16% versus ~26% decrease), but the sense of variation is similar. Concentrations of Mg, Fe, and Ca in the abraded Lemon Rind spot lie below rock-to-soil/dust mixing lines, and the datum for the brushed Lemon Rind Mg concentration lies substantially below the line (meaning that compositional variations are not simply a result of soil/dust contamination). Concentrations of Al, Si, Ti, and Mn lie along the mixing line, whereas concentrations of Na, Cl, K, and P lie above the line. As noted above, the grind on Lemon Rind was incomplete; surface materials left intact by incomplete grinding will exaggerate the differences between rind and subjacent outcrop.

[40] These data suggest that the processes involved in rind formation were similar to those proposed for veneer formation: concentration of siliciclastic residue, represented most obviously by Si and Al; precipitation of ~1.5% NaCl; and possible limited removal of sulfate minerals during weathering. Once again, the spatial distribution of rinds indicates relatively late formation. As noted above, at Shoemaker's Patio, rinds coat reoriented outcrop blocks with angular unconformity, indicating that at least some rinds developed after formation of Eagle crater (Figure 14c). In contrast, rinds on reoriented blocks at the younger Fram crater have, themselves, been reoriented, indicating emplacement before crater formation (Figure 13).

[41] Rinds are commonly developed on outcrop rocks characterized by polygonal crack networks, posited to reflect volume reduction during water loss from hydrated sulfate minerals [*Chavdarian and Sumner*, 2006; *Squyres et al.*, 2006; *Jolliff and McLennan*, 2006]. There is no close one-to-one relationship between cracks and rinds; i.e., most cracked outcrop rocks do not have rinds. Where rinds occur on cracked outcrops, however, they are cut by the same crack networks that mark subjacent outcrop. Rinds do not extend downward into cracks. These observations suggest that rinds formed after groundwater-mediated diagenesis (crystal molds persistent in rinds) and after formation of the regional plains surface. On the other hand, at least some rinds predate excavation of the relatively young Fram crater, and some formed before or contemporaneously with development of the ubiquitous polygonal crack systems.

[42] Like veneers, rinds may have formed particularly effectively at the interface between outcrop surfaces and blanketing soils. Rinds clearly develop at rock/soil interfaces, and can be well exposed at the periphery of rock surfaces that have recently been stripped of their soil cover (e.g., Figure 14). A thin soil cover could be expected to promote rind formation both by providing a medium for development of thin films of water and by protecting the developing rind from eolian abrasion. The observation that veneers in many cases postdate formation of crack systems would seem to indicate at least partial temporal separation of rinds and veneers, with rinds forming earlier, possibly during more persistent or chemically aggressive weathering conditions. We cannot tell whether rinds formed during a single short-lived episode or whether they developed slowly by intermittent interaction with thin films of water or water vapor.

6. Fracture Fill

[43] Fracture fill features are erosionally resistant, commonly vertically oriented structures closely associated with pronounced linear fractures in outcrop rock (Figures 18–20). Fin-like features of possible fracture fill origin were first observed in Eagle crater, and unambiguous fills occur within linear fractures in Endurance crater; however, for reasons of instrument arm accessibility, this class of feature was analyzed most thoroughly at target Roosevelt along the periphery of Erebus crater to the south (Figures 1 and 20 and Table 7). The features discussed here are actually developed only at the margins of fractures, indicating limited cementation of materials that accumulated in fractures (see below). These structures are spectrally distinct from adjacent outcrop [*Farrand et al.*, 2007]; like the rinds described above, they tend to have a lower albedo than surrounding outcrop, an overall "bluer" color (higher reflectance at shorter wavelengths) and a NIR absorption centered near 900 nm. Chemically, resistant fill structures differ from rinds only in detail. APXS comparison of fracture fill materials with adjacent outcrop rocks (Tables 7–9) show

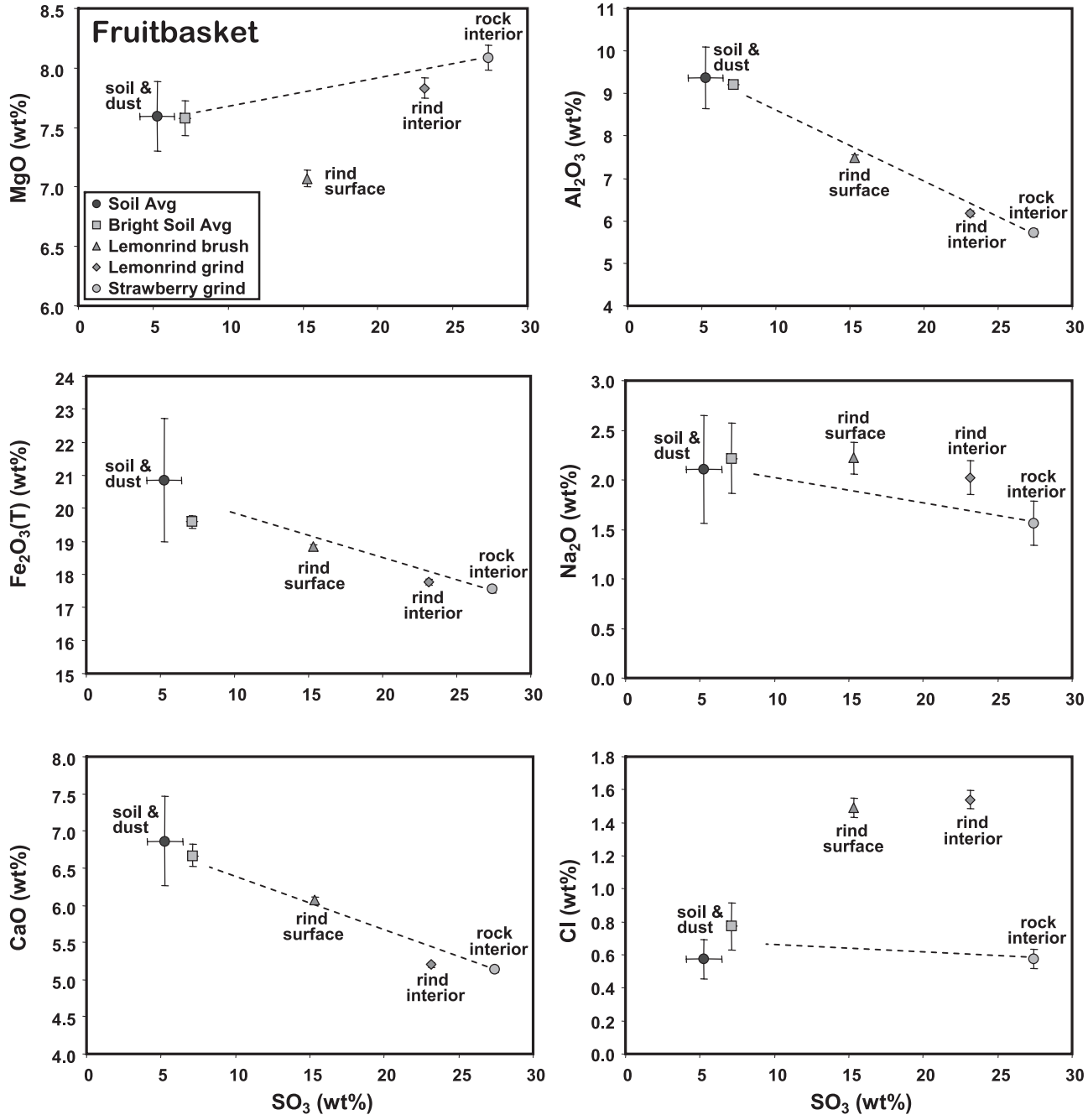

Figure 17. Fruit Basket: APXS composition of unaltered outcrop surface, brushed surface, and rock interior exposed by RAT grinding, compared with composition of regional soil/dust. The *x* axis for all plots is weight percent SO_3; the *y* axis shows weight percent abundance of selected other components; dashed lines indicate a linear mixing line between rock interior and soil/dust.

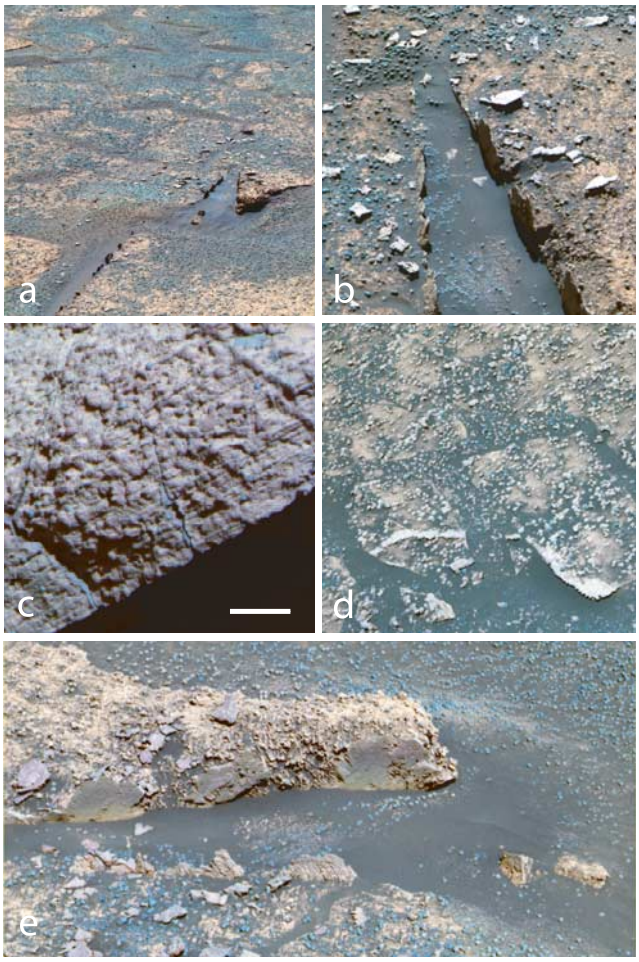

Figure 18. Fracture fill features at feature Razorback (Figures 18a, 18b, and 18e) plus variants at Ellesmere (Figure 18c) and Sermilik (Figure 18d), in Endurance crater. (a and b) Erosionally resistant ''fins'' targeted as Hogsnout (sol 152, sequence P2380, false color image acquired using Pancam L2 (753 nm), L5 (535 nm), and L7 (432 nm) filters) and (sol 170, sequence P2598, false color image acquired using Pancam L2 (753 nm), L5 (535 nm), and L7 (432 nm) filters); (c) Ellesmere; note dark thin fill in subvertical fractures (sol 206, sequence P2420, false color image acquired using Pancam L2 (753 nm), L5 (535 nm), and L7 (432 nm) filters); (d) Sermilik (sol 193, sequence P2549, false color image acquired using Pancam L2 (753 nm), L5 (535 nm), and L7 (432 nm) filters); (e) cemented fracture fill target Hogshead, (sol 175, sequence P2531, false color image acquired using Pancam L2 (753 nm), L5 (535 nm), and L7 (432 nm) filters). Bar in Figure 18c is approximately 5 cm long for Figures 18b–18e.

the by now familiar theme of SO_3 depletion (by an average of 26%); with slight enrichment of SiO_2, Al_2O_3, and Na; however, in this case the concentration of Cl (and Br) is highly variable, enriched in two and depleted in three samples. Concentrations of the cations Mg, Ca, and Fe are also variable, showing enrichments relative to adjacent rocks in some cases and depletions in others. MB data indicate a twofold olivine enrichment. We note, however, that it has been difficult to obtain a target for fracture fill structures that is free of soil or dust contamination. Because of their low relief, irregular structure, and sometimes fragile nature, these features cannot be cleaned effectively with the RAT. The apparent olivine enrichment is probably, therefore, a consequence of soil contamination.

[44] Although the compositional comparisons of fracture fill structures to nearby rock interiors vary for the different pairs sampled, the trends share general characteristics with veneers and rinds. Concentrations of Al and Si in fracture fills and fins lie along a mixing line between rock interiors and soil/dust (Figure 21). Concentrations of Mg, Ca, and Fe are depleted in some, but are highly variable. At Roosevelt, for example, Mg and Ca are depleted, as in other later stage alteration features, but Fe is actually enriched. Concentrations of P and Cl are high compared to such mixing lines, and Na and K are high for most, but not all samples.

[45] The high proportional abundance of silicates means that the fill structures are not primarily precipitates. Consistent with this hypothesis, MI images show grains within the fill (Figure 20c). There is also evidence of included spherules (Figure 18e), although whether this represents intraclastic infill or spherules plucked from (or in place in) adjacent outcrop is uncertain. An MI mosaic of the fracture fill target Rough Rider (at Roosevelt) clearly shows thin laminae, spaced about 1 mm apart from one another, that run parallel to fracture walls in resistant structures (Figure 20b). Between adjacent laminae, thin bars run perpendicular to lamination. These textures are interpreted as cement phases. The morphologically distinct fill structures are thin (a few mm), occupying only the margins of much wider

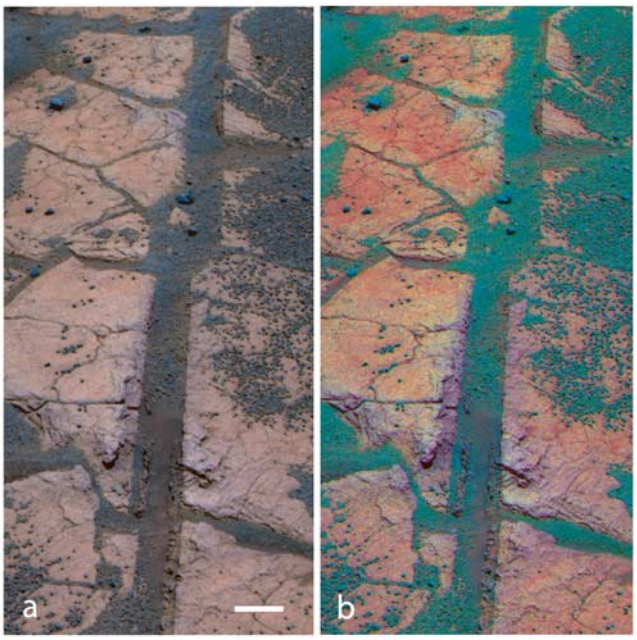

Figure 19. Fracture fill target Middrive Pancam on outcrop exposure near Olympia. (a) Sol 651, sequence P2579, false color image acquired using Pancam L2 (753 nm), L5 (535 nm), and L7 (432 nm) filters; (b) decorrelation stretch of same target. Note faint lamination in cemented fracture fill (intermittently exposed bumpy ridges interior to linear fracture walls). Bar in Figure 19b is about 5 cm.

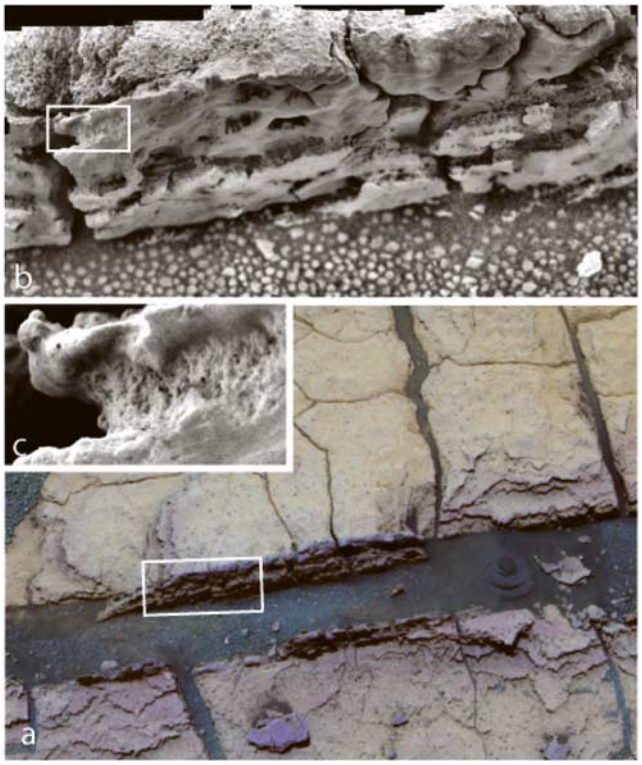

Figure 20. Fracture fill at Roosevelt (Rough Rider) at Olympia. (a) Pancam false color image of Roosevelt fracture fill (sol 731, sequence P2537, false color image acquired using Pancam L2 (753 nm), L5 (535 nm), and L7 (432 nm) filters); white box shows position of MI mosaic in Figure 20b. (b) MI mosaic, acquired while the target was in shadow on sol 727, showing adjacent outcrop rock at top, vertically laminated fracture fill in the center, and clastic grains within fracture; white box shows position of magnified image in Figure 20c; (c) magnification of a portion of the MI mosaic, showing sand grains in recessed central zone. Rectangle in Figure 20c and MI mosaic are 4 cm long.

fractures. Thus, either fractures widened after fill emplacement or the cements that conferred erosion resistance were confined to minor brines that wicked through intraclastic infill only along fracture margins.

[46] The presence of jarosite and absence of basaltic minerals, save for a small enrichment in olivine (which may result from trapped soil or dust), suggests that fractures were not filled primarily by materials comparable to present-day Meridiani soils. Indeed, the close similarity of fracture fill and country rock lithologies suggests that fractures were filled largely by intraclastic material derived from adjacent outcrops, with selective removal of one or more sulfate minerals and admixture or modern contamination by soil/dust. Fe-oxides are candidates for cement phases, as is silica–both are consistent with elemental analyses and either could impart the observed differential resistance to physical erosion.

[47] Taken collectively, Pancam observations, MI images, and chemical data are consistent with fracture formation after main phase deposition and diagenesis of Meridiani outcrop rocks. Despite the ubiquity of the polygonal crack systems noted above, conspicuous fracture fills are associated primarily with meter- to decameter-scale linear fractures that commonly occur in parallel or radial sets. Plausibly, these fractures formed in association with impact, but this remains to be demonstrated. *Chavdarian and Sumner* [2006] proposed that some physical features of Meridiani outcrop rocks can be explained in terms of physical and (partial) geochemical analog deposits at White Sands National Monument, New Mexico [see also *Grotzinger et al.*, 2005]. *Chavdarian and Sumner* [2006] illustrated polygonal cracking systems formed in eolian gypsum deposits at White Sands and hypothesized that they formed by sulfate dehydration in a low-humidity environment. Fin-like features associated with cracks were interpreted in terms of cement precipitation from brines that migrated by capillary flow through the cracks, with subsequent erosional exposure. As at Meridiani, erosionally resistant fill structures at White Sands consist of sand grains lithified by cement.

[48] *Chavdarian and Sumner*'s [2006] model for crack formation is consistent with that proposed by *McLennan et al.* [2005] for Meridiani Planum, and the fracture fill hypothesis can be applied to Meridiani rocks, as well. The most significant difference between the White Sands analog and Meridiani fracture fills is that most Meridiani fracture fill is not spatially or, it seems, genetically related to polygonal cracking. Thus, the mineral dehydration associated with widespread polygonal cracking is an unlikely source for late diagenetic brines that infiltrated Meridiani fractures. Sulfate dehydration related to impact could provide water for fluid flow through linear fracture systems.

[49] *Shinbrot et al.* [2006] alternatively proposed that Meridiani features reflect electrostatic interactions among migrating sand grains in an arid environment, but this hypothesis does not account for the fins' chemical composition, fracture-parallel laminations, well-cemented nature, or spatial relationship to linear fractures at Meridiani Planum.

[50] Two features within Endurance crater suggest a variation on the fracture fill theme. At Ellesmere and Sermilik, Opportunity imaged thin features oriented at a low angle to bedding. At Sermilik, a thin vein of light material cuts outcrop rock–it is not clear whether the vein lies in the bedding plane (Figure 18d). The Sermilik vein has spectral properties similar to "popcorn" diagenetic textures in the same target. Examples of "popcorn" materials, crushed beneath the rover's wheels, show a red hematite spectral signature in Pancam multispectral data, but we have no chemical data to evaluate this further. Pancam images of Ellesmere show a thin vein that appears to track polygonal cracking in the rock (Figure 18c). Again, in the absence of chemical or MI data, it is impossible to know what relationship these features bear to each other or to the more conspicuous fracture fills in Meridiani outcrops.

7. Discussion and Conclusions

[51] From the foregoing descriptions and interpretations, we can conclude that the alteration history of Meridiani outcrop rocks did not end with the groundwater-mediated diagenetic features described in previous publications. Veneers, rinds and fracture fill provide evidence of limited

Table 7. APXS and Mössbauer Compositions of Fracture Fill Materials[a]

	Sol				
	B051	B175	B199	B241	B727
Feature target	Real Sharks Tooth Enamel rock surface	Hoghead Arnold Ziffel frac-fill flake	Axel Heiberg Bylot Sermilik fracture fill	Ellesmere Barbeau frac surface	Roosevelt RoughRider fracture fill
			APXS Concentrations (wt %)		
SiO_2	38.3	41.5	42.2	41.5	39.9
TiO_2	0.67	0.83	0.91	0.81	0.84
Al_2O_3	6.99	7.89	7.83	7.39	7.29
Cr_2O_3	0.17	0.22	0.29	0.23	0.22
Fe_2O_3(T)	19.7	17.5	17.8	18.1	20.4
MnO	0.24	0.25	0.34	0.39	0.31
MgO	8.16	8.29	7.87	7.47	6.75
CaO	4.37	5.45	5.84	5.79	5.71
Na_2O	2.16	2.11	2.11	2.09	1.94
K_2O	0.52	0.56	0.55	0.59	0.59
$P2O_5$	0.99	0.99	0.96	0.97	1.04
SO_3	18.7	14.8	14.0	15.0	16.0
Cl	0.85	1.26	0.94	1.18	0.81
			APXS Concentrations (*ppm*)		
Ni	653	465	540	528	572
Zn	388	388	380	453	495
Br	100	108	187	1232	73
Mössbauer Phase Assignment (wt % of Fe)	B051RU0 Real Sharks Tooth_Ename1	B174RU0 Hoghead_ ArnoldZiffel	B198RU0 Bylot_ Sermilik		B726RU Roosevelt RoughRider
Olivine	1	5	6		4
Pyroxene	8	17	12		10
npOx	nu	nu	nu		nu
Jarosite	22	24	24		30
Fe3D3	15	17	20		18
Magnetite	0	0	0		0
Hematite	54	36	37		37
Fe^{3+}/FeT	0.91	0.77	0.81		0.86

[a]Here nu indicates not used in Mössbauer fit.

later weathering involving water or water vapor and at least one transient episode of brine percolation through intraclastic fill in postdepositional fracture systems. Veneers and rinds may still be forming beneath soil blankets on the Meridiani plain.

[52] All three alteration features show evidence of proportional sulfate loss and silicate gain; veneers and rinds, but not fracture fill, suggest the additional precipitation of NaCl and variable amounts of Br during alteration. *Yen et al.* [2005] proposed that the presence of Br probably indicates the activity of liquid water, perhaps as thin films episodically formed under climatic conditions where frost deposited at night could sublime in the morning and condense in cold traps. Such frost deposition was actually observed in early morning observations of the Opportunity rover deck on sol 257 [*Landis and the MER Athena Science Team*, 2007].

[53] The geochemical record of late stage alteration at Meridiani Planum indicates that environmentally informative minerals such as jarosite and hematite formed before the current plains surface formed (most likely during deposition and early diagenesis). The observations that veneers and rinds are enriched in Na and Cl but not in sulfate lends little support to hypotheses of sulfate deposition by later Hesperian or Amazonian acid fogs [*Banin et al.*, 1997]. On the other side of the planet, observations by the Spirit rover in Gusev Crater similarly suggest that acidic groundwaters deposited sulfate minerals within soils early in Martian history [*Wang et al.*, 2006].

[54] Uncertainties in absolute age make it difficult to quantify rates of erosion at Meridiani Planum, but they are undoubtedly low–the current plain is flat and thinly blanketed by dust, windborne basaltic sands, and an erosional lag of hematitic spherules. Previous interpretations of physical erosion rates [*Golombek et al.*, 2006] and soil chemistry [*Yen et al.*, 2005] at Opportunity's landing site suggest that the Meridiani plain has changed very little since current outcrop rocks were exposed. Complementary observations in Gusev Crater also indicate pronounced aqueous alteration early in Martian history, but limited further alteration during the past several billion years [*Golombek et al.*, 2006; *Hurowitz and McLennan*, 2007].

[55] The limited degree of surface alteration at Meridiani Planum despite outcrop exposure for hundreds of millions of years similarly indicate low net rates of chemical alteration, well below those measured even in arid regions of the Earth [e.g., *Ewing et al.*, 2006; *Nichols et al.*, 2006]. Collectively, veneers, rinds, and fracture fill features suggest that while water or water vapor has influenced Meridiani surfaces during the past several hundred million years (an interval at least broadly comparable to Earth's Phanerozoic Eon), that activity has been rare and transient or has operated at exceedingly low net rates.

Table 8. APXS and Mössbauer Compositions of Closest Rocks to Fracture Fill Materials[a]

	Sol				
	B045	B180	B195	B240	B696
Feature target	Flat Rock partial RAT Mojo2_RAT	Diamond Jenness Holman 3 RAT 2	Axel Heiberg Bylot Bylot_RAT	Ellesmere NoCoating	Ted RAT
			APXS Concentrations (wt %)		
SiO_2	36.3	40.1	37.9	40.4	34.6
TiO_2	0.74	0.81	0.77	0.76	0.71
Al_2O_3	6.18	6.70	6.52	7.27	5.40
Cr_2O_3	0.20	0.22	0.23	0.20	0.18
Fe_2O_3(T)	17.0	17.3	19.7	16.6	17.6
MnO	0.26	0.31	0.37	0.25	0.32
MgO	8.38	6.49	6.81	8.03	7.08
CaO	5.19	5.03	5.01	5.26	5.74
Na_2O	1.64	1.71	1.86	1.85	1.51
K_2O	0.59	0.63	0.60	0.60	0.55
$P2O_5$	1.01	1.06	1.01	1.00	1.01
SO_3	23.6	19.6	19.3	18.0	26.5
Cl	0.54	1.64	1.69	1.26	0.46
			APXS Concentrations (*ppm*)		
Ni	656	611	933	509	537
Zn	427	486	499	380	554
Br	105	14	10	395	182
Mössbauer Phase Assignment (wt % of Fe)	B045RR0 FlatRock_ Mojo2	B179RR0 DiamondJen-ness_ Holman3	B196RR0 Bylot_ Aktineq3	B241RU0 Ellesmere_ Barbeau3	B693RR Olympia Ted
Olivine	1	2	2	7	2
Pyroxene	15	11	13	17	10
npOx	nu	nu	nu	nu	nu
Jarosite	22	29	30	32	28
Fe3D3	25	18	14	17	20
Magnetite	0	0	0	0	0
Hematite	38	41	41	27	40
Olivine/pyroxene	0.07	0.18	0.15	0.41	0.20
Fe^{3+}/FeT	0.85	0.88	0.85	1	0.88

[a]Here nu indicates not used in Mössbauer fit.

Table 9. Comparison of Fracture Fill to Nearby Rock

	Fracture Fill Target							
	Real Sharks tooth enamel	Hoghead Arnold Ziffel	Axel Heiberg Bylot Sermilik	Ellesmere Barbeau	Roosevelt RoughRider	Average	SD 2-sigma	Significant?
Nearby rock	Flat Rock partial RAT	Diamond Jenness Holman 3	Axel Heiberg Bylot	Ellesmere NoCoating	Ted RAT			
			APXS (*Fracture Fill*/*Rock*)					
SiO_2	1.06	1.04	1.11	1.03	1.16	1.08	0.11	maybe
TiO_2	0.91	1.03	1.18	1.07	1.18	1.08	0.22	N
Al_2O_3	1.13	1.18	1.20	1.02	1.35	1.18	0.24	maybe
Cr_2O_3	0.83	1.02	1.25	1.12	1.22	1.09	0.34	N
Fe_2O_3(T)	1.16	1.01	0.90	1.09	1.16	1.07	0.22	N
MnO	0.94	0.79	0.91	1.57	0.97	1.04	0.61	N
MgO	0.97	1.28	1.16	0.93	0.95	1.06	0.30	N
CaO	0.84	1.08	1.17	1.10	1.00	1.04	0.25	N
Na_2O	1.32	1.23	1.13	1.13	1.29	1.22	0.18	Y
K_2O	0.88	0.89	0.92	0.98	1.07	0.95	0.16	N
$P2O_5$	0.98	0.93	0.95	0.98	1.03	0.97	0.08	N
SO_3	0.79	0.75	0.73	0.83	0.60	0.74	0.17	Y
Cl	1.56	0.77	0.56	0.94	1.77	1.12	1.05	N
SiO_2	1.00	0.76	0.58	1.04	1.07	0.89	0.42	N
TiO_2	0.91	0.80	0.76	1.19	0.89	0.91	0.34	N
Al_2O_3	0.96	7.48	18.3	3.12	0.40	6.05	14.8	variable
			Mössbauer (*Fracture Fill*/*Rock*)					
Olivine	1.0	2.5	3.0	2.0		2.2	2.1	maybe
Pyroxene	0.5	1.5	0.9	1.0		1.0	1.0	N
Jarosite	1.0	0.8	0.8	1.1		0.9	0.2	N
Fe3D3	0.6	0.9	1.4	0.9		1.0	0.8	N
Hematite	1.4	0.9	0.9	0.9		1.1	0.6	N
Olivine/pyroxene	1.9	1.6	3.3	2.0		2.2	1.8	Y
Fe^{3+}/FeT	1.1	0.9	1.0	1.0		1.0	0.2	N

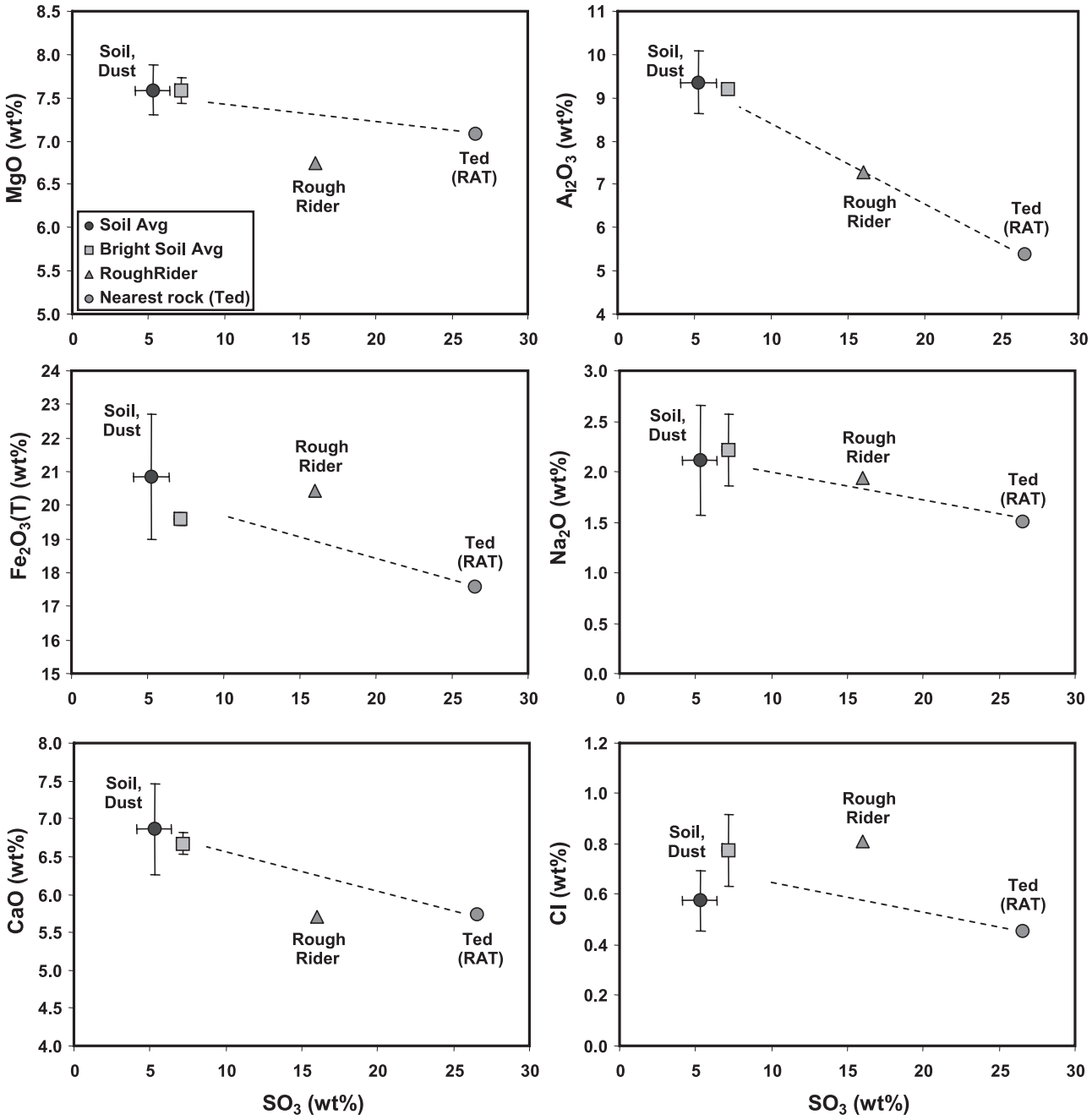

Figure 21. APXS composition of undisturbed fracture fill Roughrider (at Roosevelt) compared with the compositions of nearby outcrop target Ted and regional soil/dust. The *x* axis for all plots is weight percent SO_3; the *y* axis shows weight percent abundance of selected other components; dashed lines indicate a linear mixing line between rock interior and soil/dust. Note that Ted may or may not provide a good proxy for the source of fracture fill material preserved in Roughrider.

[56] Meridiani Planum has evidently been a biologically forbidding place for most of the time since outcrop rocks were exposed at its surface, and probably much longer. This is not incompatible with reports of contemporaneous aqueous activity elsewhere on Mars, but it does join a growing body of data and theory which suggests that liquid water has been a local, episodic and transient feature of the Martian surface for a very long time [e.g., *Gaidos and Marion*, 2003; *Shuster and Weiss*, 2005; *Richardson and Mischna*, 2005; *Hurowitz and McLennan*, 2007]. Surface environments might have been marginally and transiently habitable at the time Meridiani outcrop rocks formed [*Squyres et al.*, 2004; *Knoll et al.*, 2005], but in more recent times, the challenges to life at or near the planetary surface have only mounted. Because the persistence of life depends as much on the length of intervals between aqueous episodes as it does on the duration of liquid water when it occurs, sustained near-surface habitability of the Meridiani plain seems unlikely during the past several hundred million years.

[57] **Acknowledgments.** This is a contribution by the Athena science team for Mars Exploration Rover mission. We thank NASA for support and the many engineers and scientists involved in MER for making this mission so successful. We also thank Dawn Sumner for a most useful review.

References

Arvidson, R. E., et al. (2006), Nature and origin of the hematite-bearing plains of Terra Meridiani based on analyses of orbital and Mars Exploration rover data sets, *J. Geophys. Res.*, *111*, E12S08, doi:10.1029/2006JE002728.

Banin, A., F. X. Han, I. Kan, and A. Cicelsky (1997), Acidic volatiles and the Mars soil, *J. Geophys. Res.*, *102*, 13,341–13,356, doi:10.1029/97JE01160.

Bell, J. F., III, et al. (2003), The Mars Exploration Rover Athena Panoramic Camera (Pancam) investigation, *J. Geophys. Res.*, *108*(E12), 8063, doi:10.1029/2003JE002070.

Bell, J. F., III, et al. (2004), Pancam multispectral imaging results from the Opportunity rover at Meridiani Planum, *Science*, *306*, 1703–1709, doi:10.1126/science.1105245.

Bell, J. F., III, J. R. Joseph, J. Sohl-Dickstein, H. Arneson, M. Johnson, M. Lemmon, and D. Savransky (2006a), In-flight calibration of the Mars Exploration Rover Panoramic Camera instrument, *J. Geophys. Res.*, *111*, E02S03, doi:10.1029/2005JE002444.

Bell, J. F., III, D. Savransky, and M. J. Wolff (2006b), Chromaticity of the Martian sky as observed by the Mars Exploration Rover Pancam instruments, *J. Geophys. Res.*, *111*, E12S05, doi:10.1029/2006JE002687.

Chavdarian, G. V., and D. Y. Sumner (2006), Cracks and fins in sulfate sand: Evidence for recent mineral-atmospheric water cycling in Meridiani Planum outcrops?, *Geology*, *34*, 229–232, doi:10.1130/G22101.1.

Clark, B. C., et al. (2005), Chemistry and mineralogy of outcrops at Meridiani Planum, *Earth Planet. Sci. Lett.*, *240*, 73–94, doi:10.1016/j.epsl.2005.09.040.

Ewing, S. A., et al. (2006), A threshold in soil formation at Earth's arid-hyperarid transition, *Geochim. Cosmochim. Acta*, *70*, 5293–5322, doi:10.1016/j.gca.2006.08.020.

Farrand, W. H., et al. (2007), Visible and near-infrared multispectral analysis of rocks at Meridiani Planum, Mars, by the Mars Exploration Rover Opportunity, *J. Geophys. Res.*, *112*, E06S02, doi:10.1029/2006JE002773.

Gaidos, E., and G. Marion (2003), Geological and geochemical legacy of a cold early Mars, *J. Geophys. Res.*, *108*(E6), 5055, doi:10.1029/2002JE002000.

Gellert, R., et al. (2006), Alpha Particle X-ray Spectrometer (APXS): Results from Gusev Crater and calibration report, *J. Geophys. Res.*, *111*, E02S05, doi:10.1029/2005JE002555.

Gillespie, A. R., A. B. Kahle, and R. E. Walker (1986), Color enhancement of highly correlated images: 1. Decorrelation and HIS contrast stretches, *Remote Sens. Environ.*, *20*, 209–235, doi:10.1016/0034-4257(86)90044-1.

Goetz, W., et al. (2005), Indication of drier periods on Mars from the chemistry and mineralogy of atmospheric dust, *Nature*, *436*, 62–65, doi:10.1038/nature03807.

Golombek, M. P., et al. (2006), Erosion rates at the Mars Exploration Rover landing sites and long-term climate change on Mars, *J. Geophys. Res.*, *111*, E12S10, doi:10.1029/2006JE002754.

Gorevan, S. P., et al. (2003), The Rock Abrasion Tool: Mars Exploration Rover Mission, *J. Geophys. Res.*, *108*(E12), 8068, doi:10.1029/2003JE002061.

Grotzinger, J. P., et al. (2005), Stratigraphy and sedimentology of a dry to wet eolian depositional system, Burns Formation, Meridiani Planum, Mars, *Earth Planet. Sci. Lett.*, *240*, 11–72, doi:10.1016/j.epsl.2005.09.039.

Grotzinger, J. P., et al. (2006), Sedimentary textures formed by aqueous processes, Erebus crater, Meridiani Planum, *Geology*, *34*, 1085–1088, doi:10.1130/G22985A.1.

Hamilton, V. E., H. Y. McSween, and B. Hapke (2005), Mineralogy of Martian atmospheric dust inferred from thermal infrared spectra of aerosols, *J. Geophys. Res.*, *110*, E12006, doi:10.1029/2005JE002501.

Hartmann, W. K., and G. Neukum (2001), Cratering chronology and evolution of Mars, *Space Sci. Rev.*, *96*, 165–194, doi:10.1023/A:1011945222010.

Herkenhoff, K. E., et al. (2003), Athena microscopic imager investigation, *J. Geophys. Res.*, *108*(E12), 8065, doi:10.1029/2003JE002076.

Herkenhoff, K. E., et al. (2004), Evidence for ancient water on Meridiani Planum from Opportunity's Microscopic Imager, *Science*, *306*, 1727–1730, doi:10.1126/science.1105286.

Hurowitz, J. A., and S. M. McLennan (2007), A ~3.5 Ga record of water-limited, acidic weathering conditions on Mars, *Earth Planet. Sci. Lett.*, *260*, 432–443, doi:10.1016/j.epsl.2007.05.043.

Hynek, B. M., R. E. Arvidson, and R. J. Phillips (2002), Geologic setting and origin of Terra Meridiani hematite deposit on Mars, *J. Geophys. Res.*, *107*(E10), 5088, doi:10.1029/2002JE001891.

Jolliff, B. L., and S. M. McLennan (2006), Evidence for water at Meridiani, *Elements*, *2*, 163–169, doi:10.2113/gselements.2.3.163.

Jolliff, B. L., B. C. Clark, D. W. Mittlefehldt, and R. Gellert, and the Athena Science Team (2007), Compositions of spherules and rock surfaces at Meridiani, in *Seventh International Conference on Mars*, Abstract 3374, Jet Propul. Lab., Pasadena, Calif.

King, P. L., and H. Y. McSween (2005), Effects of H_2O, pH, and oxidation state on the stability of Fe minerals on Mars, *J. Geophys. Res.*, *110*, E12S10, doi:10.1029/2005JE002482.

Klingelhöfer, G., et al. (2003), Athena MIMOS II Mössbauer spectrometer investigation, *J. Geophys. Res.*, *108*(E12), 8067, doi:10.1029/2003JE002138.

Knoll, A. H., et al. (2005), An astrobiological perspective on Meridiani Planum, *Earth Planet. Sci. Lett.*, *240*, 179–189, doi:10.1016/j.epsl.2005.09.045.

Landis, G. A., and the MER Athena Science Team (2007), Observation of frost at the equator of Mars by the Opportunity rover, *Lunar Planet. Sci. Conf.*, XXXVIII, Abstract 2423.

Lane, M. D., P. R. Christensen, and W. K. Hartmann (2003), Utilization of the THEMIS visible and infrared imaging data for crater population studies of the Meridiani Planum landing site, *Geophys. Res. Lett.*, *30*(14), 1770, doi:10.1029/2003GL017183.

Lemmon, M., et al. (2004), Atmospheric imaging results from the Mars exploration rovers: Spirit and Opportunity, *Science*, *306*, 1753–1756, doi:10.1126/science.1104474.

McLennan, S. M., et al. (2005), Provenance and diagenesis of the evaporate-bearing Burns formation, Meridiani Planum, Mars, *Earth Planet. Sci. Lett.*, *240*, 95–121, doi:10.1016/j.epsl.2005.09.041.

McSween, H. Y., and K. Keil (2000), Mixing relationships in the Martian regolith and the composition of globally homogeneous dust, *Geochim. Cosmochim. Acta*, *64*, 2155–2166, doi:10.1016/S0016-7037(99)00401-9.

Morris, R. V., et al. (2006), Mössbauer mineralogy of rock, soil, and dust at Meridiani Planum, Mars: Opportunity's journey across sulfate-rich outcrop, basaltic sand and dust, and hematite lag deposits, *J. Geophys. Res.*, *111*, E12S15, doi:10.1029/2006JE002791.

Nichols, K. K., et al. (2006), Dates and rates of arid region geomorphic processes, *GSA Today*, *16*, 4–11, doi:10.1130/GSAT01608.1.

Richardson, M. I., and M. A. Mischna (2005), Long-term evolution of transient liquid water on Mars, *J. Geophys. Res.*, *110*, E03003, doi:10.1029/2004JE002367.

Rieder, R., R. Gellert, J. Brückner, G. Klingelhöfer, G. Dreibus, A. Yen, and S. W. Squyres (2003), The new Athena alpha particle X-ray spectrometer for the Mars Exploration Rovers, *J. Geophys. Res.*, *108*(E12), 8066, doi:10.1029/2003JE002150.

Shinbrot, T., K. LaMarche, and B. J. Glasser (2006), Triboelectrification and razorbacks: geophysical patterns produced in dry grains, *Phys. Rev. Lett.*, *96*, doi:10.1103/PhysRevLett.96.178002.

Shuster, D. L., and B. P. Weiss (2005), Martian surface paleotemperatures from thermochronology of meteorites, *Science*, *309*, 594–600, doi:10.1126/science.1113077.

Squyres, S. W., and A. H. Knoll (2005), Outcrop geology at Meridiani Planum: Introduction, *Earth Planet. Sci. Lett.*, *240*, 1–10, doi:10.1016/j.epsl.2005.09.038.

Squyres, S. W., et al. (2004), In situ evidence for an ancient aqueous environment at Meridiani Planum, Mars, *Science*, *306*, 1709–1714, doi:10.1126/science.1104559.

Squyres, S. W., et al. (2006), Two years at Meridiani Planum: Results from the Opportunity Rover, *Science*, *313*, 1403–1407, doi:10.1126/science.1130890.

Wang, A., et al. (2006), Sulfate deposition in subsurface regolith in Gusev Crater, Mars, *J. Geophys. Res.*, *111*, E02S17, doi:10.1029/2005JE002513.

Yen, A. S., et al. (2005), An integrated view of the chemistry and mineralogy of Martian soils, *Nature*, *436*, 49–54, doi:10.1038/nature03637.

Yen, A. S., et al. (2006), Evidence for halite at Meridiani Planum, *Lunar Planet. Sci. Conf.*, XXXVII, Abstract 2128.

J. F. Bell III, Z. Learner, S. W. Squyres, and R. Sullivan, Department of Astronomy, Cornell University, Ithaca, NY 14853, USA.

B. C. Clark, Lockheed Martin Corporation, 10890 Park Range Road, Littleton, CO 80127, USA.

W. H. Farrand, Space Science Institute, 4750 Walnut Street, Boulder, CO 80301, USA.

R. Gellert, Department of Physics, University of Guelph, MacNaughton Building, Gordon Street, Guelph, ON, Canada N1G 2W1.

M. P. Golombek and A. Yen, Jet Propulsion Laboratory, California Institute of Technology, MS 183-501, 4800 Oak Grove Drive, Pasadena, CA 91109, USA.

J. P. Grotzinger, Division of Geological and Planetary Sciences, California Institute of Technology, MC170-25, 1200 E. California Boulevard, Pasadena, CA 91125, USA.

K. E. Herkenhoff and J. R. Johnson, Astrogeology Team, U.S. Geological Survey, 2255 N. Gemini Drive, Flagstaff, AZ 86001, USA.

B. L. Jolliff, Department of Earth and Planetary Sciences, Washington University, Campus Box 1169,1 Brookings Drive, St. Louis, MO 63130, USA.

A. H. Knoll and N. J. Tosca, Department of Organismic and Evolutionary Biology, Harvard University, 26 Oxford Street, Cambridge, MA 02138, USA.

S. M. McLennan, Department of Geosciences, State University of New York, ESS Building, Stony Brook, NY 11794, USA.

R. Morris, NASA Johnson Space Center, Code KR, Houston, TX 77058, USA.